Development of a new cloud model for Venus (MAD-VenLA) using the Modal Aerosol Dynamics approach

Anni Määttänen, Sabrina Guilbon, Jérémie Burgalat, Franck Montmessin

To cite this version:

Anni Määttänen, Sabrina Guilbon, Jérémie Burgalat, Franck Montmessin. Development of a new cloud model for Venus (MAD-VenLA) using the Modal Aerosol Dynamics approach. Advances in Space Research, 2023, 71 (1), pp.1116-1136. 10.1016/j.asr.2022.09.063. hal-03821124

HAL Id: hal-03821124
https://hal.science/hal-03821124v1

Submitted on 9 Nov 2022

Available online at www.sciencedirect.com

ScienceDirect

Advances in Space Research xx (2022) xxx-xxx

ADVANCES IN SPACE RESEARCH
(a COSPAR publication)

www.elsevier.com/locate/asr

Development of a new cloud model for Venus (MAD-VenLA) using the Modal Aerosol Dynamics approach

Anni Määttänen[a,*], Sabrina Guilbon[b,1], Jérémie Burgalat[c], Franck Montmessin[b]

[a] *LATMOS/IPSL, Sorbonne Université, UVSQ Université Paris-Saclay, CNRS, Paris, France*
[b] *LATMOS/IPSL, UVSQ Université Paris-Saclay, Sorbonne Université, CNRS, Guyancourt, France*
[c] *GSMA, UMR CNRS 7331, U.F.R. Sciences Exactes et Naturelles, Université de Reims, Reims, France*

Received 2022; Received in final form 2022; Accepted 2022;
Available online 2022

Abstract

For decades, clouds have remained a central open question in understanding the climate system of Venus. We have developed a new microphysical model for the clouds of Venus that we describe in this paper. The model is a modal aerosol dynamical model that treats the formation and evolution of sulfuric acid solution droplets with a moderate computational cost. To this end, the microphysical equations are derived to describe the evolution of the size distribution of the particles using the moments of the distribution. We describe the derivation of the equations and their implementation in the model. We tested each microphysical process of the model separately in conditions of the Venus' atmosphere and show that the model behaves in a physically sound manner in the tested cases. The model will be coupled in the future with a Venus Global Climate Model and used for elucidating the remaining mysteries.

Keywords: Venus clouds; Microphysical modeling; Sulfuric acid aerosols

---

1. Introduction

Models are crucial for understanding the role of clouds in the climate of Venus, since the observations of Venus clouds are scarce. The only *in situ* descent profile that measured the cloud properties and their vertical distribution comes from Pioneer Venus (Knollenberg & Hunten, 1980). Until recently, the Venus International Reference Atmosphere (VIRA, Kliore et al., 1985) that aggregated and merged all existing datasets into a reference model of the Venusian atmosphere, was also the baseline for atmospheric model comparisons and provided important inputs also for cloud models (temperature and pressure profiles). The European Space Agency mission Venus Express (VEx, 2005-2014) shed more light on the atmosphere of Venus and characterized the climate, in particular the structure of the atmosphere in terms of temperature and density, concentrations of trace gases, and even winds (Limaye et al., 2018; Marcq et al., 2018). The properties of the upper cloud and the upper haze were measured by VEx with several observation methods, revealing new aspects of the Venus cloud droplet distribution (Titov et al., 2018). However, the

---

[*] Corresponding author: email: anni.maattanen@latmos.ipsl.fr

[1] Currently at: Dennemeyer & Co. Sàrl, Luxembourg

https://dx.doi.org/10.1016/j.jasr.xxxx.xx.xxx

properties of the middle and the lower cloud layers can not be easily probed with remote sensing observations mainly because of the high optical thickness of the clouds, and thus VEx was not able to replace the unique descent profile of Pioneer Venus as the reference for cloud properties.

Pioneer Venus probe's Cloud Particle Size Spectrometer (LPSC) instrument revealed the structure of the cloud layers (Knollenberg & Hunten, 1980). The clouds of Venus can be divided in three layers of varying properties, with hazes surrounding the cloud layers above and below. The particle size distributions in the clouds were found to have at least two modes, and a third, larger mode was observed in the lowest cloud layer. The mean radii and variances of the modes and their variation as a function of altitude were also established (Knollenberg & Hunten, 1980): modes 1 and 2, respectively, for small (r=0.2 μm) and medium particles (r=1.0 μm), and the third mode that would contain the largest particles (r=3.5 μm). The composition and existence of the latter mode, detected by the Pioneer Venus probe, are still debated. Since then, these observations have been the reference on the structure of the Venus' cloud layers and the particle size distributions, particularly for the lowest cloud layers that are difficult to observe via satellite. Other particle modes have been suggested in interpretation of measurements, such as mode 0 (smaller than mode 1) and mode 2' (larger than mode 2), but the prevailing standard in the community is to use the LSPC measurements as the reference (see reviews in Esposito et al., 1983, 1997; Titov et al., 2018)

Several microphysical models have been developed for the Venus' clouds to understand better the formation and evolution of the cloud layers that cover the whole planet and have a fundamental effect on its climate. The models have been developed since the 1980s for different purposes, mainly to help in interpreting observations. In particular in the 1990s and 2000s, four models were published (James et al., 1997; Imamura & Hashimoto, 1998; Yamamoto & Takahashi, 2006; McGouldrick & Toon, 2007). The latest published model (Gao et al., 2014; Parkinson et al., 2015a,b) is based on a newer version of the same model that James et al. (1997) and McGouldrick & Toon (2007) used (CARMA, Toon et al., 1988). None of these models have been used in a three-dimensional (3D) context.

In general, these microphysical models can be divided in two groups: sectional models and modal models. The difference between the two is the way to describe the particle size distribution: either by discretizing the distribution in sections or bins as a function of particle size, or by fixing the size distribution shape and describing the integral properties of the distribution, such as the total number of particles, the average radius and the total volume. Most of these models consider liquid, spherical sulfuric acid solution droplets. The assumption of sphericity eases radiative transfer calculations and is very probably a good estimate for the Venusian particle shape unless solid particles exist. The models also often include a source of condensation nuclei (CN) that help in forming the droplets.

To our knowledge, the first published model was a 1D model by Toon et al. (1982), which is a sectional model coupled to a chemistry module. It allowed for the formation of sulfur allotropes (S_x) up to S_8 and included the coagulation between the liquid sulfuric acid solution droplets and the sulfur particles S_x. Thus the model was able to form two particle populations of mixed composition and it had the ability to follow the fractions of the components, like it was the case for the terrestrial models developed in the same epoch (Turco et al., 1979) and on which the Toon et al. (1982) model was based. However, the model was not able to reproduce the observed cloud properties. For example, at 62 km altitude, the model of Toon et al. (1982), despite obtaining a bimodal distribution, does not reproduce the tail of the small particles of mode 1 and underestimates the observed number concentration in the clouds. However, this study initiated the further development of several Venus versions of the same model (James et al., 1997; McGouldrick & Toon, 2007; Gao et al., 2014) with different levels of complexity.

Imamura & Hashimoto (2001), using their sectional model, highlighted the importance of atmospheric circulation for the comprehension of Venus' cloud system. Likewise, McGouldrick & Toon (2007) studied this issue and showed that their model produced results that much better corresponded to the observed clouds when atmospheric dynamics was included at a sufficient detail. Only accounting for the vertical (eddy) transport, such as is usually done in a 1D model, did not suffice for an accurate modeling of large-scale cloud structures.

In addition to the sectional models listed above, three published models use a different parameterization of the particle size distribution. The simplified particle size description of Hashimoto & Abe (2001) is based on determining the mean radius and the particle number density for a unimodal size distribution in equilibrium with its environment. Mass fluxes of sulfuric acid and water between the different atmospheric layers are calculated and these fluxes are then used to calculate the number concentration of droplets as a function of particle size (modes 2 or 3 of Knollenberg & Hunten (1980)). Coagulation is applied via a parameter that varies with altitude. The model is based on Krasnopolsky & Pollack (1994) who tried to model atmospheric chemistry within the clouds, and the same parameterizations are used in the Global Climate Model (GCM) of Lee et al. (2010).

Two modal models have been previously developed using the moment method (Yamamoto & Tanaka, 1998; Yamamoto & Takahashi, 2006) These two models describe only the liquid droplet mode 1. The particle size distribution is supposed to have a lognormal shape and its standard deviation is fixed in one of the models (Yamamoto & Takahashi, 2006) but not in the other (Yamamoto & Tanaka, 1998), meaning that the latter model has more prognostic variables than the former so that the freely varying standard deviation can be calculated. However, the simplified model of Yamamoto & Takahashi (2006) led to an unsatisfactory correspondence between the model and the observations by Pioneer Venus (Knollenberg & Hunten, 1980). The authors indicated the reason being the simplified nucleation scheme of their model that does not produce enough particles.

Although none of the models perfectly reproduce the Pioneer Venus observations, these studies led to different hypotheses on the origin of the UV absorber (polysulfur, Toon et al., 1982), impact of clouds on the radiative budget (McGouldrick & Toon, 2007) and the understanding of the chemical cycles within the clouds (H_2O-H_2SO_4 cycle: Krasnopolsky & Pollack, 1994). Some models also introduce CN to help in forming the clouds. However, some models do not explicitly define the nature of the CN (McGouldrick & Toon, 2007), and others put forward hypotheses of sulfur aerosols or meteoric dust particles (Gao et al., 2014).

To help elucidate the untamed mysteries of Venus' clouds, a modal microphysical model, called MAD-VenLA (Modal Aerosol Dynamics for Venus Liquid Aerosols), has been developed and is presented in this article. The ultimate goal is to integrate in the future MAD-VenLA into the Global Climate Model for Venus of the Institute Pierre-Simon Laplace (IPSL-VGCM, Lebonnois et al., 2010) to be able to conduct global 3D simulations of Venus' cloud microphysics. The VGCM includes currently a cloud parameterization of (Stolzenbach, 2016): however, it does not contain microphysical processes and only describes clouds in equilibrium with their environment. For the microphysical model, the choice of the moment method allows us to limit the number of tracers to be added to the VGCM due to the integration of the cloud model. Modal models are very often used in terrestrial GCMs (Vignati et al., 2004; Mann et al., 2010) and also already used in the Titan and Mars GCMs (Burgalat et al., 2014; Navarro et al., 2014; Haberle et al., 2019; Määttänen et al., 2022). This method offers a good compromise between the accuracy of the results and the computational time.

This article reports the derivations of the mathematical expressions of the microphysical equations with moments, developed particularly for Venus' clouds, that have been implemented in MAD-VenLA. The governing equations for all of the microphysical processes acting in the model are presented, with a part of the detailed derivations given in an Appendix. We also report and discuss the hypotheses that were necessary for the development of the model. We study the behavior of the model processes one by one in an idealized 0D setting in Venus' atmospheric conditions and show that the modal parameterization performs as expected. Direct comparison with observations is not done here since our model does not include transport nor radiative transfer, for which coupling with a VGCM will be necessary and will be performed in the future.

2. Materials and Methods

In this section we describe the model and the expressions developed in this work for the case of Venus' aerosols. We start with the description of the moment method applied to a particle size distribution and continue with the descriptions of the different aerosol dynamical processes accounted for in the model. Only the derivations of the main expressions are retained in the article and the detailed derivations can be found in Appendix A, together with two additional processes (aerosol production and sedimentation) that are needed if the model is used in a 1D setting (Appendix B).

2.1. Moments of a lognormal particle size distribution

A moment M of the kth order, noted as M_k, is an integrated quantity that can be generally expressed as the integral of a function $f(x)$ on an inteval $I \subset \Re^+$. In our case, the function $f(x)$ is the particle number concentration $n(r)$ as a function of radius r (the particle size distribution). We can then write the moment of the kth order of this size distribution as:

$$M_k = \int_0^\infty r^k n(r) dr. \tag{1}$$

Applied to a lognormal function used for Venus' cloud size distributions, and noting M_0 the total particle concentration, we can write

$$M_k = M_0 \bar{r}_g^k \exp\left(\frac{k^2 \ln^2(\sigma_g)}{2}\right) \tag{2}$$

with $\bar{r}_g$, σ_g and M_0 being the median radius, geometric standard deviation and the zeroth moment of the distribution (equal to the total number of particles of the distribution).

We have decided to fix the standard deviation of our lognormal size distributions. This allows us, with the help of Eq. (2), to define a parameter $\alpha(k)$:

$$\alpha(k) = \exp\left(\frac{k^2 \ln^2(\sigma_g)}{2}\right) \tag{3}$$

so that $M_k = M_0 \bar{r}_g^k \alpha(k)$. With this latter expression we can calculate any moment of the kth order as a function of the zeroth order moment M_0.

2.2. Modeled modes and moments of the size distribution

MAD-VenLA accounts for three lognormal size distributions, two of which describe the liquid cloud droplets (the observed modes 1 and 2) and the third the preexisting aerosols that act as condensation nuclei (CN). The lognormal form of the size distributions, their number and the size ranges they describe are based on the Pioneer Venus nephelometer measurements (Knollenberg & Hunten, 1980) and previous modeling work. Concerning the preexisting solid aerosols that can function as CN, we suppose that their density is 2000 kg m^{-3} as estimated for meteoric dust particles (Hunten et al., 1980). In this model version we do not account for the Mode 3 of Knollenberg & Hunten (1980).

The three distributions are described with the help of two moments: M_0, equal to the total particle number, and M_3, proportional to the total volume of the particles. We chose these two moments (M_0 and M_3) since they represent convenient characteristics of the particle size distribution. In the development of the moment method equations, a moment of any order k can be calculated from M_0

with the help of the term $\alpha(k)$ defined above. Equation (2) shows the dependence of the moments on the median radius and on the standard deviation. In reality, the standard deviation of a particle size distribution can vary. However, letting the standard deviation vary in the model would increase the number of moments, and in addition, its variations can not be verified with the existing observations. Choosing only two moments is permitted by the definition of a constant standard deviation of our size distribution, the value of which has been chosen based on observations (Table 1). This also allows us to simplify the equations of the model (Yamamoto & Takahashi, 2006; Burgalat et al., 2014). Thus, in the model we have two moments (M_0, M_3) for each of the three modes, adding up to six moments in total.

Table 1. Parameters of the mode 1 and 2 size distributions on Venus used in our model. The values are based on the Pioneer Venus measurements (Knollenberg & Hunten, 1980).

Mode	**Standard deviation**	**Radius (m)**
1	1.56	$3.0 \cdot 10^{-7}$
2	1.29	$1.0 \cdot 10^{-6}$

For each droplet the amount of acid and water are followed independently. We also keep track of the condensation nuclei (solid, activated aerosols: CN) potentially existing inside the droplets. Thus, the third moment is a sum of three moments: $M_3 = M_3^{(H_2SO_4)} + M_3^{(H_2O)} + M_3^{CN}$, where the sum $M_3^{(H_2SO_4)} + M_3^{(H_2O)}$ corresponds to the liquid part of the droplet. The volumes of acid and water are given by the composition of the droplet, calculated in the next section (2.3). Similarly, the zeroth moment is a sum of two moments: M_0^{drop} the total number of liquid particles and M_0^{CN} the total number of CN activated in the droplets. Thus, $M_0 = M_0^{drop} + M_0^{CN}$. For the size distribution of the solid, unactivated aerosols we apply the appropriate moments (M_0^{aer} and M_3^{aer}).

This sums up as 12 moments in total. When this model will be used in a GCM, these 12 moments will be the 12 tracers that the GCM will need to advect. As a comparison, integrating in a GCM some of the other, published Venus cloud models such as Imamura & Hashimoto (1998) or Gao et al. (2014), would require 23 or 45 tracers, respectively. This means that using the moment method will help in limiting the computational cost of the simulations.

2.3. Weight percent of sulfuric acid in the droplets

On Venus the droplets in modes 1 and 2 are liquid droplets composed of a sulfuric acid solution. The composition is given by the acid mass fraction in the droplet:

$$W_m = \frac{m_a}{m_a + m_w}. \tag{4}$$

where m_a and m_w are, respectively, the condensed masses of sulfuric acid and water. The droplet composition is mainly controlled by the temperature and the relative humidity (Steele & Hamill, 1981; James et al., 1997). We calculate separately the composition for each of the two modes by using the Ridders method that solves by double iteration the Kelvin equation and simultaneously conserves the total mass of water in the system (Stolzenbach, 2016). Following Hashimoto & Abe (2001) and Stolzenbach (2016), we assume that the composition does not depend on the particle size. We have verified this hypothesis by calculating the weight percent of acid in a set of conditions valid for Venus (see Table 2).

The weight percent of acid remains nearly constant for all droplet radii in all conditions, as shown in Fig.1. A small variation is seen for case 3 where the weight percent for 1 nm particles is about 1.6% larger than for larger droplets (>10 nm). As these sizes correspond to the freshly nucleated particles that grow very fast, and the majority of the observed particles in the atmosphere are of the order of 100 nm to 1 μm, we consider this deviation negligible for our model. Thus, in MAD-VenLA the weight percent does not vary with particle size but only with water vapor concentration. In what follows, the weight percent will be calculated solely for the median radius of the size distribution.

Table 2. Conditions used for calculating the variation of the acid weight percent in the cloud droplets.

Parameter	Lower cloud (Case 1)	Middle cloud (Case 2)	Upper cloud (Case 3)
Altitude (km)	48	54	60
Temperature (K)	366	312	262
Pressure (hPa)	1375	616	236
H_2SO_4 (ppmv)	6.93	0.08	1.0
H_2O (ppmv)	20	15	1

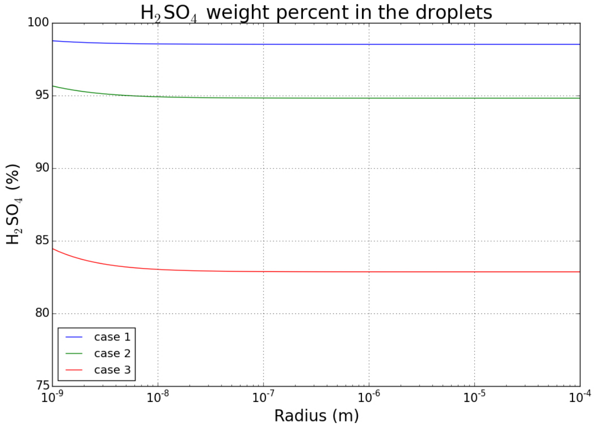

Fig. 1. Variation of the weight percent of sulfuric acid in the atmosphere of Venus as a function of droplet radius for the cases listed in Table 2.

We will also need the weight percent of acid in a droplet in equilibrium with its environment. This parameter is defined as

$$W_m^{eq} = \frac{m_a}{m_a + m_w + \Delta m_w} \tag{5}$$

where Δm_w is the mass of water that needs to be added to the droplet to obtain the equilibrium composition.

2.4. Homogeneous nucleation

We calculate the homogeneous nucleation rate J_{hom} of sulfuric acid and water with the parametrization of Määttänen et al. (2018). The nucleation rate of droplets of the critical size r^* (critical radius) is given by $J_{hom}(r^*)$ that then converts to a temporal variation of the number density of droplets $n(r)$:

$$\frac{dn(r)}{dt} = J_{hom}(r^*)\delta_{r^*}(r) \tag{6}$$

where $\delta_{r^*}(r)$ is a Dirac peak centered on r^*. First, Equation (6) is integrated over all the radii of the distribution, and then by multiplying with r^k we get:

$$\frac{d}{dt}\int_0^\infty n(r)r^k dr = \int_0^\infty J_{hom}(r^*)r^k\delta_{r^*}(r)dr. \tag{7}$$

We introduce M_k, the moment of kth order, in the equation to obtain:

$$\frac{dM_k}{dt} = J_{hom}(r^*)r^{*k} \tag{8}$$

where r^* is the critical radius of the droplets. By discretizing the equation and expressing the moment M_k at the timestep $t+1$, we get the the following relation:

$$M_{k,t+1} = J_{hom}(r^*)r^{*k}\Delta t + M_{k,t}. \tag{9}$$

2.5. Heterogeneous nucleation

We can similarly express the heterogeneous nucleation with moments. We note n_{aer} the number distribution of unactivated aerosols in the atmosphere, n_{CN} that of the CN (the number of activated aerosols on which the liquid droplets can form), and J_{het} the heterogeneous nucleation rate. We can write the number of droplets created by heterogeneous nucleation as:

$$\frac{dn_{CN}(r)}{dt} = J_{het}(r) 4\pi r^2 n_{aer}(r) \tag{10}$$

where r is the radius of the CN.

We integrate Equation (10) over the radius space so that we can express it with the help of moments :

$$\frac{d}{dt} M_k^{CN} = J_{het} 4\pi M_{k+2}^{aer} \tag{11}$$

Applying to the distribution the definition of a moment of the kth order and Eq. (3) we can write:

$$M_{k+2}^{aer} = M_k^{aer} \bar{r}_{\mathrm{aer}}^2 \frac{\alpha(k+2)}{\alpha(k)}. \tag{12}$$

Here $\bar{r}_{\mathrm{aer}}$ is the median radius of the aerosol size distribution. The number of produced CN is equal to the number of aerosols lost to nucleation:

$$\frac{dM_k^{CN}}{dt} = 4\pi J_{het} \bar{r}_{\mathrm{aer}}^2 \frac{\alpha(k+2)}{\alpha(k)} M_k^{aer} = -\frac{dM_k^{aer}}{dt}. \tag{13}$$

The new aerosol mode moments at timestep $t+1$ are given by

$$M_{k,t+1}^{aer} = \frac{1}{1 + (4\pi J_{het} \bar{r}_{\mathrm{aer}}^2 \frac{\alpha(k+2)}{\alpha(k)})\Delta t} M_{k,t}^{aer}. \tag{14}$$

The heterogeneous nucleation rate is calculated via a simple activation of the aerosols. We use the approach of James et al. (1997). We calculate for each size bin of a pre-defined aerosol size grid the saturation ratio S over a droplet of the same size accounting for the Kelvin effect and the actual vapor concentrations. When the saturation ratio exceeds unity for a given radius, all of the aerosols in this size bin are activated and are transformed into droplets. The aerosol size distribution is comprised of 100 bins, guaranteeing a sufficient precision of the activated fraction of aerosols in our sensitivity tests (see Appendix A.1.1). The nucleation subroutine is the only one in MAD-VenLA not using the moment method, as it is impossible to express the activation in moments. This parametrization was compared with a more detailed expression (see Appendix A.1.1) and was deemed sufficient, especially due to the unknown properties of the venusian CN, inhibiting the correct use of the classical expression for heterogeneous nucleation. The routine can be improved in the future if precise information on the nature and properties of the CN can be acquired and the classical nucleation theory can be used to express the nucleation rate.

2.6. Mass transfer

On Venus the size of the two-component solution cloud droplets evolves through the mass transfer (condensation or evaporation) of sulfuric acid and water. The fluxes of the two vapors are steered by two processes. The droplets remain in thermodynamical equilibrium by adjustment to the equilibrium composition when the environmental conditions change. The equilibrium adjustment happens through exchange of water between the droplet and its environment. Water pilots this process due to its concentration being higher than that of sulfuric acid in the atmosphere of Venus, leading to more frequent collisions of water molecules with the droplet. Thus, it is assumed that the mass of sulfuric acid in the droplet stays constant in the equilibrium adjustment. Once the droplet is in its equilibrium composition (defined by the temperature and the relative humidity), it might still be sub- or supersaturated with respect to sulfuric acid. In this case condensation or evaporation – conserving the equilibrium composition – will lead to a change in its size. This process is dominated by sulfuric acid flux, and the corresponding water flux is defined by the conservation of the equilibrium composition.

Following James et al. (1997) and Steele & Hamill (1981), the change in the mass of the binary water-sulfuric acid droplet m_g can be written:

$$\frac{dm_g(r)}{dt} = \underbrace{\left.\frac{dm_a(r)}{dt}\right|_{W_m^{eq}} + \left.\frac{dm_w(r)}{dt}\right|_{W_m^{eq}}}_{\left.\frac{dm_g(r)}{dt}\right|_{W_m^{eq}}} + \frac{\Delta m_w(r)}{\tau} \tag{15}$$

where τ is the model time step, m_a and m_w are respectively the condensed masses of sulfuric acid and water in the droplet, and m_g the total condensed mass in the droplet so that $m_g = m_a + m_w$.

The first term on the right hand side of Eq. (15) represents the change in the sulfuric acid mass generated by condensation or evaporation, the second term the change in the mass of water from condensation/evaporation, and the last term gives the variation of the water mass due to the equilibrium adjustment.

As mentioned before, we suppose that the water and acid fractions in the droplet do not depend on the droplet size. We will note the mass fraction of sulfuric acid in the droplet as $W_m = m_a/(m_a + m_w)$. Then $m_a = W_m m_g$, since the total mass of the droplet $m_g = m_a + m_w$. With Eq. (5), we can write : $\Delta m_w = (m_a + m_w)(W_m/W_m^{eq} - 1)$. These expressions allow us to rewrite Eq. (15):

$$\frac{dm_g}{dt} = \frac{1}{W_m^{eq}} \left.\frac{dm_a}{dt}\right|_{W_m^{eq}} + \frac{m_g}{\tau}\left(\frac{W_m}{W_m^{eq}} - 1\right). \tag{16}$$

Thus, the temporal variations of the droplet mass m_g are governed by sulfuric acid, and then the change in acid mass is used for calculating the quantity of water required to adjust the droplet into equilibrium with its environment.

Condensation and evaporation change the total mass and volume of a droplet size distribution, and this is why the mass flux changes only the third order moment that is proportional to the volume. The total number of particles, given by M_0, does not change, except when all droplets evaporate. We need to express the change in M_3 and for doing so we will start from the equation of mass transfer for sulfuric acid:

$$\left.\frac{dm_a}{dt}\right|_{W_m^{eq}} = 4\pi\rho_a r \frac{S_a - S_a^*}{R_c + R_d} = 4\pi\rho_a r^2 \frac{dr}{dt} \tag{17}$$

where R_c and R_d are the resistances to growth by heat conduction and diffusion (Kuroda, 1984), and S_a^* is the saturation ratio of sulfuric acid at the droplet surface given by the Kelvin equation $S^* = \exp\left((2e_s v_1)/(k_B T r^*)\right)$. In the Kelvin equation, e_s is the surface tension (calculated with the approach of Vehkamäki et al., 2002; Vehkamäki et al., 2003), v_1 the volume of a molecule, k_B the Boltzmann constant, T the temperature and r^* the radius of the droplet. To find an analytical solution to this equation in moments, we apply a second order Taylor-Young expansion of S_a^* to obtain an expression using powers of r that we can integrate:

$$S_a^* = B - \frac{A}{r_0^2}B(r - r_0) + \frac{(r - r_0)^2}{2}B\left(\frac{2A}{r_0^3} + \frac{A^2}{r_0^4}\right) \tag{18}$$

where the parameters A and B are

$$A = \frac{2e_s M_a}{\rho_a RT} \tag{19}$$

$$B = \exp\left(\frac{A}{r_0}\right) \tag{20}$$

with M_a the molar mass of sulfuric acid and ρ_a the density of the condensate. We can rewrite the equation (16) as a function of moments:

$$\frac{dM_3}{dt} = \left.\frac{dM_3}{dt}\right|_{W_m^{eq}} + \frac{M_3}{\tau}\left(\frac{W_m}{W_m^{eq}} - 1\right) \tag{21}$$

and

$$\left.\frac{dM_3}{dt}\right|_{W_m^{eq}} = \int_0^\infty 3r\frac{S_a - S_a^*}{R_c + R_d}n(r)dr \tag{22}$$

since for W_m^{eq}, the variation of M_3 is also governed by the growth rate $g(r)$ related to sulfuric acid. Taking the Taylor expansion of S_a^* (Equation 18), we obtain:

$$\left.\frac{dM_3}{dt}\right|_{W_m^{eq}} = a_1M_1 + a_2M_2 + a_3M_3 \tag{23}$$

with the coefficients a_1, a_2 et a_3:

$$a_1 = \left[S - B - \frac{AB}{r_0} - \frac{r_0^2AB}{2}\frac{2r_0 + A}{r_0^4}\right]\frac{3}{R_c + R_d} \tag{24}$$

$$a_2 = \left[\frac{AB}{r_0^3}(A + 3r_0)\right]\frac{3}{R_c + R_d} \tag{25}$$

$$a_3 = \left[-\frac{AB(2r_0 + A)}{2r_0^4}\right]\frac{3}{R_c + R_d}. \tag{26}$$

Here the median radius of the distribution, r_0, is determined at the previous time step and it is considered constant until the recalculation of its value in the end of the microphysical loop. With Eq. (3), we can define the coefficients $\alpha(1)$, $\alpha(2)$ and $\alpha(3)$ to write

$$M_1 = \bar{r}_g^{-2}\frac{\alpha(1)}{\alpha(3)}M_3 \tag{27}$$

$$M_2 = \bar{r}_g^{-1}\frac{\alpha(2)}{\alpha(3)}M_3, \tag{28}$$

and the Equation (22) becomes:

$$\left.\frac{dM_3}{dt}\right|_{W_m^{eq}} = \left(a_1\bar{r}_g^{-2}\frac{\alpha(1)}{\alpha(3)} + a_2\bar{r}_g^{-1}\frac{\alpha(2)}{\alpha(3)} + a_3\right)M_3. \tag{29}$$

We can rewrite Eq. (29) with the help of a new coefficient a_4 and express the third order moment at time $t + 1$:

$$M_{3,t+1}^g = \frac{1}{1 - a_4\Delta t}M_{3,t}^g \tag{30}$$

where

$$a_4 = \left(a_1\bar{r}_g^{-2}\frac{\alpha(1)}{\alpha(3)} + a_2\bar{r}_g^{-1}\frac{\alpha(2)}{\alpha(3)} + a_3\right) + \frac{1}{\tau}\left(\frac{W_m}{W_m^{eq}} - 1\right). \tag{31}$$

Now all of the tendencies of the third order moment M_3 of the size distribution can be calculated. As the moment M_3 is the sum of two specific moments for water and sulfuric acid, we need to calculate a coefficient that gives the fraction of mass gained/lost in each of the species-specific moments. This fraction X_m allows to distribute the tendency ($dM_3^g = M_{3,t+1}^g - M_{3,t}^g$) so that the equilibrium mass fraction of acid in conserved:

$$X_m = \frac{W_m^{eq}(dM_3^g + M_{3,t}^{H_2SO_4} + M_{3,t}^{H_2O})}{W_m(M_{3,t}^{H_2SO_4} + M_{3,t}^{H_2O})dM_3^g}. \tag{32}$$

Using the second order Taylor expansion for describing the behavior of the Kelvin equation should be taken with caution as it deviates significantly from the exact result for particle radii far from the median radius r_0. The second order Taylor expansion generates high S_a^* values for bigger particles, while it should tend towards unity. This results in an overestimation of the supersaturation in the mass transfer scheme for the largest particles when the median radius of the distribution, r_0, is small.

In addition, the supersaturation will be underestimated for very small particles. Since nucleation is calculated in our model with a parametrization, the approximation does not affect this process. However, when the size distribution moves towards smaller sizes during evaporation, the evaporation process will be slightly affected by the approximation, as the saturation ratio for the smaller tail of the distribution particles will be smaller than given by the exact solution.

As particle size distributions span several orders of magnitude in size, the errors for the mass flux for the tails of the distribution can be significant. However, only small amount of particles are contained in the tails of the distribution and thus the subsequent error may turn out to be small. The error could be reduced in theory by using very narrow distributions, which would limit the impact. As the particle modes in the model are defined for the conditions in Venus' clouds, in particular through setting the standard deviations of the modes as constant values given by observations, we can not try and limit the impact of the approximation by using narrower modes.

Despite these limitations we use this approximation in this version of the model, but we acknowledge the existence of a large deviation in supersaturation in the tails of the size distribution caused by our approximation. We have verified that the approximation is in an acceptable range (less than a factor of two) from the exact solution for a large part of the distribution, but the tails of the distribution will be subject to the increasing error of the approximation. However, the actual number of particles in the tails of the distribution that will have unexpectedly large growth rates is very small, and qualitatively the model results do not show unphysical behavior in the tests made here.

In future work our model will be developed further and we will investigate the best way of describing the saturation ratio in our model.

2.7. Coagulation

Coagulation processes in our model include only Brownian coagulation, coalescence being for the moment neglected. The equations developed for coagulation need to account for the flow regime and the particle mode in question. In the following we present the main equations for coagulation, and a part of the detailed derivations are given in Appendix A.2. These equations have been adapted for the case of Venus (two modes of spherical aerosols) from Burgalat & Rannou (2017) who developed the equations for a spherical particle mode and a fractal particle mode in Titan's atmosphere.

2.7.1. Integrated equations and the bimodal distribution

We can write the coagulation equation as a function of moments as follows (Whitby & McMurry, 1997):

$$\begin{aligned}\frac{dM_k}{dt} &= \underbrace{\frac{1}{2}\int_0^\infty\int_0^\infty \beta(r_i,r_j)(r_i^3+r_j^3)^{\frac{k}{3}}n(r_i)n(r_j)dr_idr_j}_{gain} \\ &\quad \underbrace{-\frac{1}{2}\int_0^\infty\int_0^\infty \beta(r_i,r_j)(r_i^k+r_j^k)n(r_i)n(r_j)dr_idr_j}_{loss}\end{aligned} \tag{33}$$

with M_k the k^{th} order moment, β the coagulation coefficient (also called the coagulation kernel) that depends on intra- and inter-modal interactions, r_i and r_j are the radii of the coagulating droplets and n the number distribution of the droplets of radius r_i or r_j.

In our case we consider a bimodal distribution. This allows us to write $n(r_i) = n_1(r_i) + n_2(r_i)$ where the indices 1 and 2 correspond to the respective modes. The equation (33) can thus be rewritten as follows:

$$\begin{aligned}\frac{dM_k}{dt} &= \frac{1}{2}\int_0^\infty \int_0^\infty \beta(r_i, r_j)(r_i^3 + r_j^3)^{\frac{k}{3}} \\ &\times[n_1(r_i) + n_2(r_i)][n_1(r_j) + n_2(r_j)]dr_i dr_j \\ &-\frac{1}{2}\int_0^\infty \int_0^\infty \beta(r_i, r_j)(r_i^k + r_j^k) \\ &\times[n_1(r_i) + n_2(r_i)][n_1(r_j) + n_2(r_j)]dr_i dr_j. \end{aligned} \tag{34}$$

The equation (34) will now be written for each of the considered modes and as a function of the inter- and intra-modal interactions between the droplets. Thus we define the following conventions:

1. For intra-modal interactions, in which the two coagulating droplets belong to the same mode, the droplets form a new, larger droplet that stays in that mode:
   - (mode 1 ↔ mode 1) ⇒ mode 1,
   - (mode 2 ↔ mode 2) ⇒ mode 2.
2. For inter-modal interactions, in which the two coagulating droplets belong to different modes (1 and 2), the droplets form a new, larger droplet that is assigned to the larger mode (2):
   - (mode 1 ↔ mode 2) ⇒ mode 2.

These conventions have the following implications. First, in inter-modal coagulation, mode 1 will lose its particles to mode 2. Second, in intra-model interactions the mean radius of the mode increases. For intra-modal coagulation in mode 1 in particular this means that at some point modes 1 and 2 may overlap if the mean radius of mode 1 becomes sufficiently large. To maintain two distinct modes in such a situation requires a way to handle particle transport between modes. The method of mode-merging we are using in the model for this purpose will be described later in Section 2.8.

Here, we use β to designate the coagulation coefficient in general, independently of the flow regime or the form of interaction. The terms β_{11}, β_{12} and β_{22} will represent the coefficients for the different types of intra- and inter-modal coagulation.

Thus we obtain the temporal variation of the k^{th} order moment for the intra-modal interactions:

$$\begin{aligned}\left.\frac{dM_k}{dt}\right|_{11} &= \frac{1}{2}\int_0^\infty \int_0^\infty \beta_{11}(r_i, r_j)[(r_i^3 + r_j^3)^{\frac{k}{3}} \\ &-r_i^k - r_j^k]n_1(r_i)n_1(r_j)dr_i dr_j \end{aligned} \tag{35}$$

$$\begin{aligned}\left.\frac{dM_k}{dt}\right|_{22} &= \frac{1}{2}\int_0^\infty \int_0^\infty \beta_{22}(r_i, r_j)[(r_i^3 + r_j^3)^{\frac{k}{3}} \\ &-r_i^k - r_j^k]n_2(r_i)n_2(r_j)dr_i dr_j \end{aligned} \tag{36}$$

and for inter-modal coagulation:

$$\begin{aligned}\left.\frac{dM_k}{dt}\right|_{12} &= \int_0^\infty \int_0^\infty \beta_{12}(r_i, r_j)[(r_i^3 + r_j^3)^{\frac{k}{3}} \\ &-r_i^k - r_j^k]n_1(r_i)n_2(r_j)dr_i dr_j. \end{aligned} \tag{37}$$

The process of coagulation leads to a change in the total number of droplets, and the total volume of the droplets remains constant. It can be seen that when $k = 0$, the equation (37) gives the variation of the 0^{th} order moment, which is not equal to zero. When $k = 3$, we obtain the variation of the 3^{rd} order moment, equal to zero.

Equation (37), the tendency of the moments for inter-modal coagulation where all resulting droplets end up in mode 2, can be decomposed into three components: mode 1 (m1) losses (Eq. (38)), mode 2 (m2) losses (Eq. (39)) and mode 2 gain (Eq. (40)):

$$\left.\frac{dM_k^{m1}}{dt}\right|_{12}^{L} = \int_0^\infty \int_0^\infty \beta_{12}(r_i, r_j)(-r_i^k) n_1(r_i) n_2(r_j) dr_i dr_j \tag{38}$$

$$\left.\frac{dM_k^{m2}}{dt}\right|_{12}^{L} = \int_0^\infty \int_0^\infty \beta_{12}(r_i, r_j)(-r_j^k) n_1(r_i) n_2(r_j) dr_i dr_j \tag{39}$$

$$\left.\frac{dM_k^{m2}}{dt}\right|_{12}^{G} = \int_0^\infty \int_0^\infty \beta_{12}(r_i, r_j)(r_i^3 + r_j^3)^{\frac{k}{3}} n_1(r_i) n_2(r_j) dr_i dr_j. \tag{40}$$

Now we wish to write the tendencies of the moments for modes 1 and 2 by taking into account both inter- and intra-modal interactions. We get for mode 1

$$\frac{dM_k^{m1}}{dt} = \tag{41}$$

$$\begin{aligned}
&\frac{1}{2}\int_0^\infty \int_0^\infty \beta_{11}(r_i, r_j)[(r_i^3 + r_j^3)^{\frac{k}{3}} - r_i^k - r_j^k] \\
&\times n_1(r_i) n_1(r_j) dr_i dr_j \\
&+ \int_0^\infty \int_0^\infty \beta_{12}(r_i, r_j)(-r_i^k) n_1(r_i) n_2(r_j) dr_i dr_j
\end{aligned} \tag{42}$$

and for mode 2

$$\begin{aligned}
\frac{dM_k^{m2}}{dt} = &\frac{1}{2}\int_0^\infty \int_0^\infty \beta_{22}(r_i, r_j)[(r_i^3 + r_j^3)^{\frac{k}{3}} - r_i^k - r_j^k] \\
&\times n_2(r_i) n_2(r_j) dr_i dr_j \\
&+ \int_0^\infty \int_0^\infty \beta_{12}(r_i, r_j)[(r_i^3 + r_j^3)^{\frac{k}{3}} - r_j^k] \\
&\times n_1(r_i) n_2(r_j) dr_i dr_j.
\end{aligned} \tag{43}$$

2.7.2. Coagulation coefficient or coagulation kernel

In our model we only consider Brownian coagulation. The coagulation coefficient β defines the collision and agglomeration efficiency between two droplets of radii r_i and r_j (with $i \neq j$). The coagulation coefficient will thus depend on the size of the two droplets and on the flow regime in which they are embedded. The Knudsen number, K_n, defines the flow regime with the help of the mean free path λ_g and the droplet radius r_g: $K_n = \lambda_g / r_g$. From here onwards, we note the continuum regime ($K_n \leq 1$) as CO and the free molecular regime ($K_n \gg 1$) as FM, and β_{CO} and β_{FM} the coagulation coefficients for these regimes.

In the continuum regime, the coagulation coefficient β_{CO} is expressed with the help of the droplet radii r_i et r_j and the diffusion coefficients D_i et D_j given by Eq. (44).

$$D = \frac{k_B T}{6\pi\mu_{air} r}(1 + A_{CM} K_n), \tag{44}$$

where μ is the air viscosity. Here we use an approximation of the Cunningham-Milikan correction ($1 + A_{CM} K_n$, where $A_{CM} = 1.591$; Park et al. (1999)) that allows for the transition between the flow regimes. Burgalat (2012) has estimated that the error due to the approximation $1 + A_{CM} K_n$ is between -4 and +9 % for K_n between 0.1 and 20. With this approximation we can express the diffusion coefficient in powers of r and write the coagulation equations in moments.

We can write the coagulation coefficient as follows:

$$\beta_{CO}(r_i, r_j) = 4\pi(r_i + r_j)(D_i + D_j) \tag{45}$$

with D_i and D_j the diffusion coefficients related to the droplets i et j and defined by Eq. (44). Eq. (45) is only valid in the continuum regime since it does not take into account the Fuchs interpolation that would allow for the utilisation of this equation in all flow regimes. If we note $C = A_{CM}\lambda_g$ and $K_{CO} = \frac{2k_BT}{3\mu}$ and write the coagulation coefficient as a function of radius r, we get:

$$\beta_{CO}(r_i, r_j) = K_{CO}\left[2 + \frac{r_i}{r_j} + \frac{r_j}{r_i} + C\left(\frac{1}{r_i} + \frac{1}{r_j} + \frac{r_i}{r_j^2} + \frac{r_j}{r_i^2}\right)\right] \tag{46}$$

Here the terms in r^k can then be replaced with the corresponding moments.

In the free molecular regime the coagulation coefficient β_{FM} is a function of the droplet density ρ_g (Friedlander et al., 2000):

$$\beta_{FM}(r_i, r_j) = \sqrt{\frac{6k_BT}{\rho_g}}(r_i + r_j)^2\sqrt{r_i^{-3} + r_j^{-3}} \tag{47}$$

The term $\sqrt{r_i^{-3} + r_j^{-3}}$ can not be expressed in r^k. To be able to proceed with the development of the equations on moments, we need to approximate this term following Lee & Chen (1984) who introduced a term b_k and wrote: $\sqrt{r_i^{-3} + r_j^{-3}} = b_k(r_i^{-3/2} + r_j^{-3/2})$. We also note $K_{FM} = \sqrt{\frac{6k_BT}{\rho_g}}$. Now we can rewrite Eq. (47) as follows:

$$\begin{aligned}\beta_{FM}(r_i, r_j) &= K_{FM}b_k(r_i^{1/2} + r_j^{1/2} + r_i^2 r_j^{-3/2} \\ &\quad + r_i^{-3/2}r_j^2 + 2r_i^{-1/2}r_j + 2r_i r_j^{-1/2}).\end{aligned} \tag{48}$$

Lee & Chen (1984) studied a monomodal distribution and deduced that the value of the coefficient b_k depends on the law used for the particle size distribution, its geometric standard deviation σ_g and of the order k of the moment (Table A.8). We need to define b_k for our bimodal distribution. The derivation and the choice of the values of b_k can be found in Appendix A.2.1. The final chosen values for the b_k coefficients are given in Table 3.

Table 3. The values of b_k (for moment k) chosen for our model. The superscripts T[1-4] indicate the interaction type as follows. $T1$: mode 1 intra-modal interactions; $T2$: mode 1 inter-modal interactions; $T3$: mode 2 intra-modal interactions; T4: mode 2 inter-modal interactions.

Interactions	Value
b_0^{T1}	0.73
b_0^{T2}	0.88
b_3^{T2}	0.80
b_0^{T3}	0.77

2.7.3. General expression for the tendencies of 0th and 3rd order moments

Starting from equations (42) et (43), we can determine the 0th and 3rd order moment tendencies for mode 1 ($m1$) and mode 2 ($m2$) in the different flow regimes. For the 0th order moment of the two modes we get

$$\begin{aligned}\frac{dM_0^{m1}}{dt} &= -\frac{1}{2}\int_0^\infty\int_0^\infty \beta_{11}(r_i, r_j)n_1(r_i)n_1(r_j)dr_i dr_j \\ &\quad -\int_0^\infty\int_0^\infty \beta_{12}(r_i, r_j)n_1(r_i)n_2(r_j)dr_i dr_j\end{aligned} \tag{49}$$

$$\frac{dM_0^{m2}}{dt} = -\frac{1}{2}\int_0^\infty\int_0^\infty \beta_{22}(r_i, r_j)n_2(r_i)n_2(r_j)dr_i dr_j. \tag{50}$$

Similarly, we will write the 3rd order moment for the two modes:

$$\frac{dM_3^{m1}}{dt} = \int_0^\infty \int_0^\infty \beta_{12}(r_i, r_j)(-r_i^3) n_1(r_i) n_2(r_j) dr_i dr_j \tag{51}$$

$$\frac{dM_3^{m2}}{dt} = \int_0^\infty \int_0^\infty \beta_{12}(r_i, r_j) r_i^3 n_1(r_i) n_2(r_j) dr_i dr_j. \tag{52}$$

Inter-modal coagulation will make mode 1 lose volume that will be acquired by mode 2. Thus, we can write

$$\frac{dM_3^{m2}}{dt} = -\frac{dM_3^{m1}}{dt}. \tag{53}$$

The tendencies of 0th and 3rd order moments for modes 1 and 2 as a function of the flow regime and their derivations can be found in Appendix A.2.2 and in Tables A.9 and A.10.

2.7.4. Transition regime and the harmonic mean

The transition between the free molecular regime and the continuum regime is not well-defined theoretically, but it can be estimated (semi-)empirically (Fuchs, 1964; Otto et al., 1999). For developing our model, we will use the approach of harmonic means used by Park et al. (1999). The harmonic means for a k^{th} order moment can be written:

$$\frac{dM_k}{dt} = \frac{dM_k/dt\,|_{CO} \times dM_k/dt\,|_{FM}}{dM_k/dt\,|_{CO} + dM_k/dt\,|_{FM}}. \tag{54}$$

We can also write:

$$K = \frac{K\,|_{CO} \times K\,|_{FM}}{K\,|_{CO} + K\,|_{FM}} \tag{55}$$

In order to determine the harmonic means for each mode and moment, we need to start with the equations presented in Table A.9. First we isolate inter- and intra-modal interactions and then apply Eq. (55). Doing so, we obtain the variations of the 0th and 3rd order moments. For the 0th order moment for mode 1 we obtain:

$$\begin{aligned}\frac{dM_0^{m1}}{dt} &= \frac{\gamma_{0,CO}^{m1,A01} \times \gamma_{0,FM}^{m1,A01}}{\gamma_{0,CO}^{m1,A01} + \gamma_{0,FM}^{m1,A01}} (M_0^{m1})^2 \\ &\quad - \frac{\gamma_{0,CO}^{m1,B01} \times \gamma_{0,FM}^{m1,B01}}{\gamma_{0,CO}^{m1,B01} + \gamma_{0,FM}^{m1,B01}} M_0^{m1} M_0^{m2}\end{aligned} \tag{56}$$

and for mode 2:

$$\frac{dM_0^{m2}}{dt} = \frac{\gamma_{0,CO}^{m2} \times \gamma_{0,FM}^{m2}}{\gamma_{0,CO}^{m2} + \gamma_{0,FM}^{m2}} (M_0^{m2})^2 \tag{57}$$

For the 3rd order moment, we acquire for mode 1:

$$\frac{dM_3^{m1}}{dt} = -\frac{\gamma_{3,CO}^{m1} \times \gamma_{3,FM}^{m1}}{\gamma_{3,CO}^{m1} + \gamma_{3,FM}^{m1}} M_3^{m1} M_3^{m2} \tag{58}$$

and for mode 2:

$$\frac{dM_3^{m2}}{dt} = \frac{\gamma_{3,CO}^{m1} \times \gamma_{3,FM}^{m1}}{\gamma_{3,CO}^{m1} + \gamma_{3,FM}^{m1}} M_3^{m1} M_3^{m2} = -\frac{dM_3^{m1}}{dt} \tag{59}$$

2.8. Mode-merging

As mentioned before, we describe the shape of the particle size distribution with a lognormal function so that we can apply the moment method to the microphysical equations. We use two particle modes whose mean radii evolve due to the microphysical processes. As the particles in mode 1 grow, the mode 1 radius might become similar in size or even larger than the mode 2 median radius. In such a situation, particles should be moved from the smaller mode to the larger one. In order to do this, we will apply the so-called mode-merging technique (Whitby et al., 2002) that will allow us to limit the superposition of the two modes.

We will show here the expressions for calculating the new droplet number concentrations and radii in a situation where the droplets in mode 1 are large enough to migrate in mode 2. For the mode 1 moment tendencies we can write:

$$M^{m1}_{k,t+1} = M^{m1}_{0,t}\bar{r}_1^k \exp(\frac{k^2}{2}\ln^2\sigma_1)\frac{1}{2}\Big[1+erf(u_X(k))\Big] \tag{60}$$

$$M^{m1}_{q,t+1} = M^{m1}_{0,t}\bar{r}_1^q \exp(\frac{q^2}{2}\ln^2\sigma_1)\frac{1}{2}\Big[1+erf(u_X(q))\Big] \tag{61}$$

where k and q are the orders of the moments with $k \neq q$ and the error function $erf(x)$ is defined as $erf(x) = 2/\sqrt{\pi}\int_0^x e^{-t^2}dt$. The function $u_X(k)$ is defined as:

$$u_X(k) = \frac{\ln(r_{edge}) - \ln(r_i) - k\ln^2(\sigma_i)}{\sqrt{2}\ln(\sigma_i)} \tag{62}$$

where i is the studied mode and r_{edge} the threshold radius defined as $r_{edge} = \sqrt{r_{f1}r_{f2}}$. Here, the expected median radii of the modes 1 and 2 r_{f1} and r_{f2} are respectively fixed at 330 nm and 1 μm, following the values measured by Pioneer Venus Knollenberg & Hunten (1980). This combination of equations gives us the new droplet number concentrations N_g and median radii $\bar{r}_\mathrm{g}$ of the mode as defined by Whitby et al. (2002):

$$\bar{r}_{1,t+1} = \bar{r}_{1,t}\left(\frac{1+erf(u_X(q))}{1+erf(u_X(k))}\right)^{-1/(k-q)} \tag{63}$$

and

$$N_{1,t+1} = \frac{N_{1,t}}{2}\frac{(1+erf(u_X(q)))^{k/(k-q)}}{(1+erf(u_X(k)))^{q/(k-q)}} \tag{64}$$

The same process is applied to mode 2 (with the help of the parameters calculated for mode 1), so that:

$$M^{m2}_{k,t+1} = M^{m1}_{0,t}\bar{r}_1^k \exp(\frac{k^2}{2}\ln^2\sigma_1)\frac{1}{2}\Big[1-erf(u_X(k))\Big] \tag{65}$$

$$M^{m2}_{q,t+1} = M^{m1}_{0,t}\bar{r}_1^q \exp(\frac{q^2}{2}\ln^2\sigma_1)\frac{1}{2}\Big[1-erf(u_X(q))\Big] \tag{66}$$

with k and q the orders of the moments. This provides us:

$$\begin{aligned}\bar{r}_{2,t+1} &= \bar{r}_{1,t}\exp\left(\frac{k+q}{2}(\ln^2\sigma_1 - \ln^2\sigma_2)\right)\\ &\times\left(\frac{1-erf(u_X(q))}{1-erf(u_X(k))}\right)^{-1/(k-q)}\end{aligned} \tag{67}$$

and

$$\begin{aligned}N_{2,t+1} &= \frac{N_{1,t}}{2}\exp\left(\frac{-kq}{2}(\ln^2\sigma_1 - \ln^2\sigma_2)\right)\\ &\times\frac{(1-erf(u_X(q)))^{k/(k-q)}}{(1-erf(u_X(k)))^{q/(k-q)}}\end{aligned} \tag{68}$$

In the case shown above, mode 1 loses droplets to mode 2, but the equations can also be applied to the inverse situation where mode 2 particles decrease in size and migrate to mode 1.

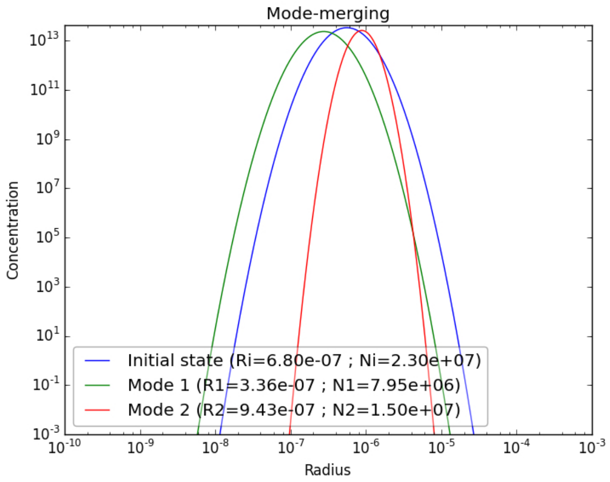

Fig. 2. An example of mode-merging results obtained with the MAD-VenLA model in 0D. The initial mode (in blue) has the same standard deviation as mode 1 ($\sigma_i = \sigma_1$). When its median radius reaches the threshold radius (r_{edge} = 570 nm) , the mode is divided in two (modes 1 and 2: respectively, in green and red). The legend gives the mean radii and total number concentrations of the size distributions (i: initial; 1: mode 1; 2: mode 2).

3. Results

We have explored the behavior of the model by testing the microphysical processes one by one in the conditions of the atmosphere of Venus in 0D. The goal of these tests was to make sure the developed routines behave as expected. The simulations are very short as in all cases a steady state is rapidly reached.

In order to test the reliability of our model, we define some basic simulations where we use a realistic reference profile of the Venus' tropical atmosphere for all of the tests (VIRA, Fig. 3, Kliore et al., 1985). This profile was chosen as it gives the closest description of the atmosphere in which Pioneer Venus descended while measuring the properties of the clouds. It provides the temperature and pressure at the altitudes chosen for the specific tests, whereas the vapor concentrations are taken from other sources (specified separately for each test case).

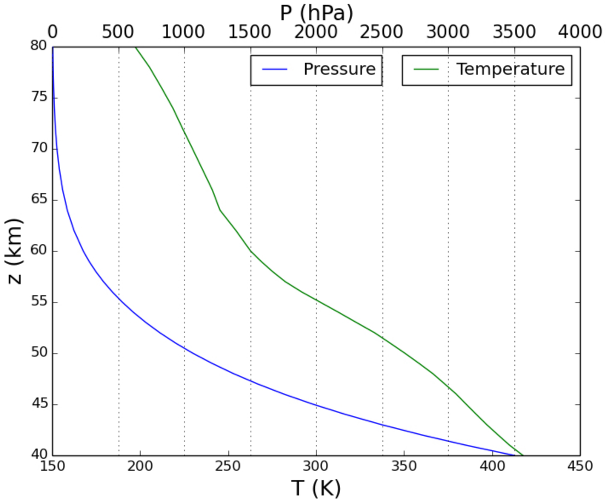

Fig. 3. VIRA pressure and temperature profiles for latitudes 0-30°.

3.1. Homogeneous and heterogeneous nucleation

The homogeneous nucleation rate is calculated with the parametrization of Määttänen et al. (2018) that depends on the relative humidity, the saturation ratio of sulfuric acid and the temperature. Figure 4 shows the results of a homogeneous nucleation test in the atmospheric conditions given in Table 4. The final concentration of the formed particles (after 3600 s) is the same for the two runs having different time steps of 1 s (typical nucleation timescale) or 15 min (typical Global Climate Model physics timestep). As changes in vapor concentrations due to nucleation are negligible, nucleation rate stays fairly constant during the simulation as the thermodynamic conditions do not vary significantly during the 1 s timestep.

Table 4. The initial conditions of the homogeneous nucleation tests. The values are based on a VIRA profile for latitude 30°N and are taken at approximately 60 km altitude.

Parameter	**Value**
Temperature (K)	262.8
Pressure (hPa)	235.7
H_2SO_4 vapor (ppmv)	$6.9 \cdot 10^{-5}$
H_2O vapor (ppmv)	1.0
Particle concentration (m_{air}^{-3})	$4.0 \cdot 10^{7}$
W_m	0.87

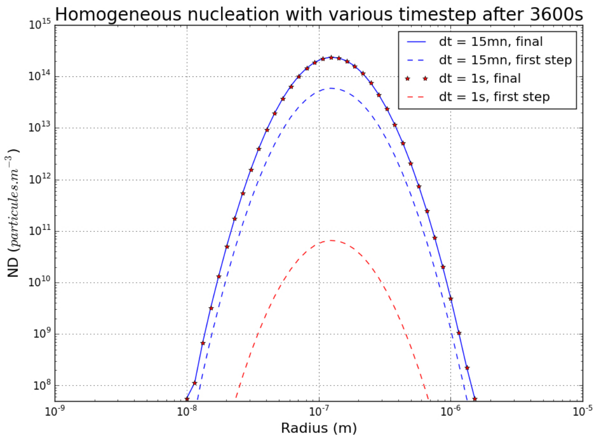

Fig. 4. Particle concentration in a 3600 s simulation with homogeneous nucleation for two different timesteps: 15 min (blue) and 1 s (red). The results after the first timestep are shown by the dashed lines and the final results (at 3600 s) with the solid lines. The initial conditions are given in Table 4.

The presence of a substrate (the CN) facilitates droplet formation via heterogeneous nucleation. We made a second test, taking three different sets of conditions (Table 5) and we calculated both homogeneous and heterogeneous nucleation in these conditions. Only heterogeneous nucleation produces droplets (Fig. 5), the homogeneous nucleation rate remaining negligible in these conditions. One should note that the homogeneous nucleation parameterization neglects nucleation rates below 0.1 cm^{-3} and is valid only for relative humidities above 10^{-5} (the value at 50 km is lower than that). At 60 and 70 km, heterogeneous nucleation starts when the saturation ratio exceeds a value above unity (1.05 in the three cases of Table 5). The nucleation rate is close to the total number of aerosols available as CN ($1.86 \cdot 10^{8}$ m^{-3} at 50 km) and reaches the maximum rate at a saturation ratio of 1.14 at all levels. It can be seen that the nucleation rate increases more rapidly at 50 km than at higher altitudes, due to the slightly different conditions. However, the differences are negligible and in practice all aerosols are activated as CN at all layers in these simulations.

Table 5. Parameters for the heterogeneous nucleation tests. Temperature T, pressure P; sulfuric acid and water vapor mixing ratios and relative humidity (RH) for the three studied altitudes (50, 60 and 70 km). The values have been taken from Stolzenbach (2016) and from a VIRA profile for latitudes 0-30°. The relative humidity has been calculated from the other values.

Altitude (km)	T (K)	P (Pa)	H_2SO_4 (ppmv)	H_2O (ppmv)	RH (%)
50	350.5	$10.7 \cdot 10^4$	0.26	20	$5.0 \cdot 10^{-5}$
60	262.8	$23.6 \cdot 10^3$	0.75	10	$8.5 \cdot 10^{-4}$
70	229.8	$36.9 \cdot 10^2$	0.09	4.5	$1.3 \cdot 10^{-3}$

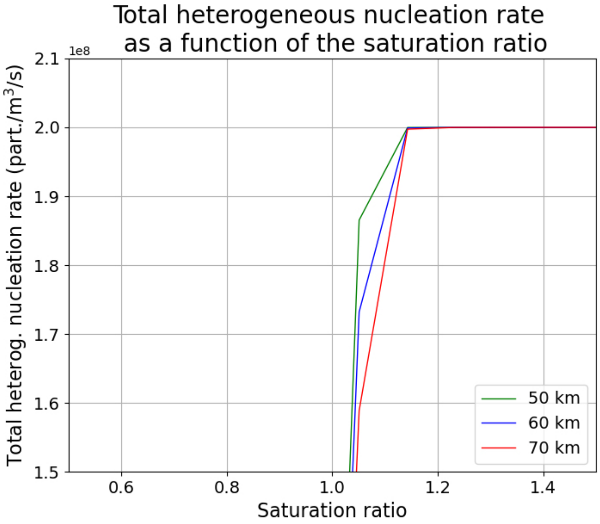

Fig. 5. Heterogeneous nucleation rate (J_{het}) as a function of the sulfuric acid saturation ratio for the three altitudes in the atmosphere of Venus given in Table 5. The initial aerosol number concentration is $2.0 \cdot 10^8$ m^{-3} and the saturation ratio varies from 0.5 to 1.5. A nucleation rate is calculated for each particle size in a 1000-bin radius grid in the range [1.0 nm,10.0 μm] and the total nucleation rate is the sum of the activated aerosols over the entire distribution.

3.2. Mass transfer

We have also conducted tests of mass transfer (condensation/evaporation) in the conditions of the atmosphere of Venus, once again taking the pressure and temperature from the VIRA profile (Fig. 3) and the vapor mixing ratios are taken as in Table 6. The choice of the latter leads to a supersaturation (S>1) for 57.5-79.5 km altitude and a subsaturation (S<1) below 57.5 km. For growth to happen, droplets need to exist, and thus we initialize the mode 1 distribution in the model prior to the mass transfer calculations. No other process is included, there is no vertical transport (sedimentation, mixing) and the output timestep is 1 s. Mass transfer affects only the particle volume (3rd order moment), and does not change the total number of particles (0th order moment, M_0) except when all particles evaporate leading to $M_0 = 0$.

Table 6. Initial profiles of gaseous sulfuric acid and water vapor for the mass transfer test cases (Stolzenbach, 2016).

Altitude (km)	H_2O (ppmv)	H_2SO_4 (ppmv)
40 - 60	15.0	0.01
60 - 80	3.0	0.01

Figures 6 and 7 show that at 55.5 km and 57.5 km the median radius of the size distribution and the total volume decrease during the simulation until complete evaporation of the droplets. This is due to the subsaturated conditions in the very warm conditions in these layers that lead to evaporation. The acceleration of the evaporation with decreasing particle radius is due to the Kelvin effect: the saturation vapor pressure increases with decreasing particle size, increasing the subsaturation and the evaporation rate as the particle size gets smaller. At higher altitudes, from 59.5 to 70.5 km, the median radius and the total volume increase with time since they evolve in supersaturated conditions. The evolution of the droplets is not similar at different altitudes. At all three altitudes the volume and the radius of the particles already grow at the start of the simulation, but then the growth stops and the particle size and volume stabilize to a constant value. This corresponds to the situation where all of the available vapor has been consumed by condensation, and since the vapor is not replenished by transport, phase equilibrium is reached. This stationary state is reached at different times, depending on the growth rate and the amount of available vapor (supersaturation) at the respective altitudes. The largest overall growth is modeled at around 60 km altitude where the thermodynamic conditions are the most favorable.

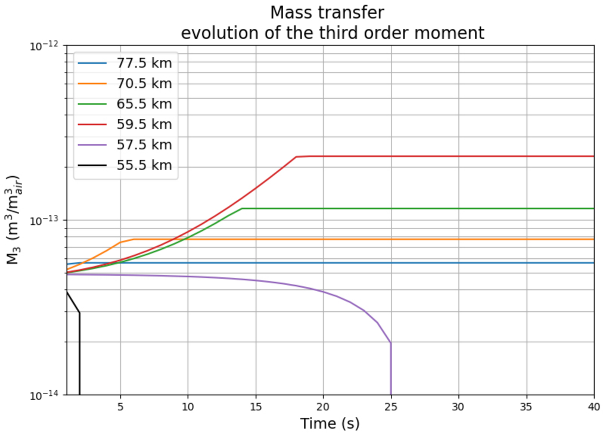

Fig. 6. Evolution of the 3rd order moment of mode 1 (proportional to the total volume of the mode) at different altitudes on Venus in the pure mass transfer test. The temperature and pressure come from the VIRA profile for latitudes 0-30° (Fig. 3).

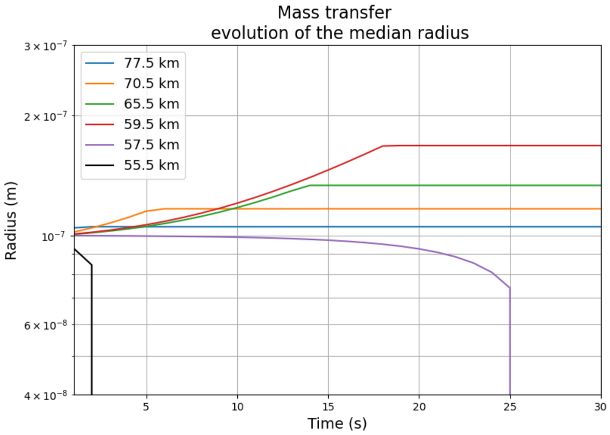

Fig. 7. Evolution of the median radius of mode 1 at different altitudes on Venus in the pure mass transfer test. The temperature and pressure come from the VIRA profile for latitudes 0-30° (Fig. 3).

In the previous test we only followed the growth/evaporation of mode 1 particles. If we include mode-merging, we can obtain growth on mode 1 particles into mode 2 thanks to the inter-mode transfer of particles made possible by this technique. This results in a decrease of the total particle number (moment M_0) of mode 1. Due to the large difference in the particle numbers of the two modes, this decrease is not very clearly visible at 65.5 km in Fig. 8, but the mode 1 decrease is equal to the visible increase of the total droplet concentration in mode 2. The increase in mode 2 is very rapid during the first 200 s (going from 0 to $3{\cdot}10^7$ m^{-3}) and continues more slowly and attains $4.5{\cdot}10^7$ m^{-3} after 1000 s.

During growth, the largest particles of mode 1 move to mode 2 and this can be seen in the behavior of the 3rd order moment M_3

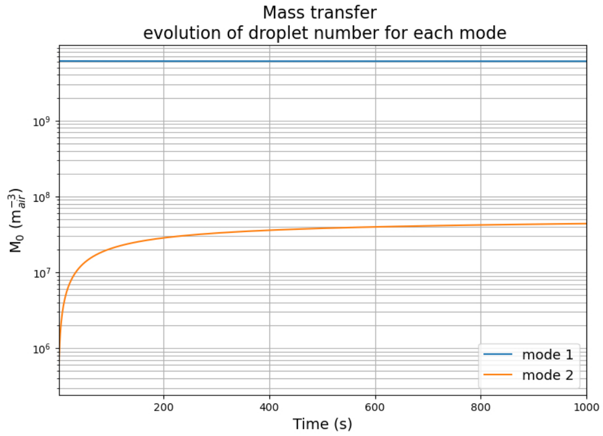

Fig. 8. Evolution of the 0th order moment (proportional to the total number of particles) of modes 1 and 2 in the test including both condensation and mode-merging at 65.5 km altitude on Venus. At the start of the simulation only mode 1 contains droplets and mode 2 acquires droplets through mode-merging.

that is proportional to the total volume of the distribution (Fig. 9). For mode 1, the M_3 moment decreases more rapidly than M_0 (Figures 8 and 9). This can be understood as $M_3 \propto \bar{r}^3_{pg} M_0$ and the M_3 of mode 1 decreases with the median radius of mode 1. The median radius of mode 2 (Fig. 10) stabilizes just like the moments M_0 and M_3.

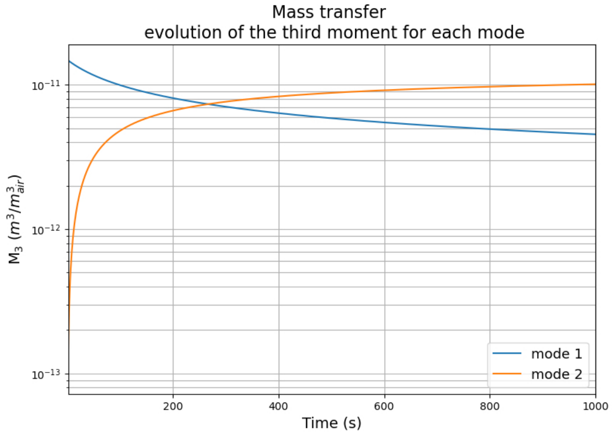

Fig. 9. Evolution of the 3rd order moment (proportional to the total volume) of modes 1 and 2 in the test including both condensation and mode-merging at 65.5 km altitude on Venus. At the start of the simulation only mode 1 contains droplets.

3.3. Impact of Brownian coagulation and mode-merging

Finally, we have conducted simulations to test coagulation and mode-merging together. The tests were made in conditions over different altitudes (40-80 km), but the results were very similar for all altitudes. Thus we have decided to choose one altitude only, 55 km, for which we present results here (see conditions in Table 7). As mentioned related to condensation, in our simulations mode 2 is not initialized but forms as a results of mode 1 particle growth and mode-merging that moves the droplets too large for mode 1 into mode 2. Here we investigate the growth process with coagulation. Intra-modal coagulation in mode 1 leads to the growth of the radius of mode 1 and eventually a part of the mode 1 particles will be moved to mode 2 by mode-merging. Once mode 2 has formed, both intra- and inter-modal coagulation can take place. Both of these processes lead to the formation of mode 2 particles and thus induce an increase in the mode 2 total droplet concentration and a decrease of the mode 1 total droplet concentration (Fig. 11). Fig. 12 shows that the median radius of mode 2 varies very little and that the increase of M_3 is governed here only by the

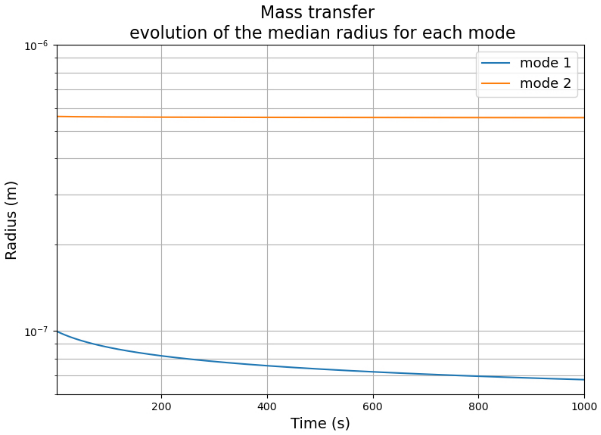

Fig. 10. Variation of the median radius of modes 1 and 2 in the test including both condensation and mode-merging at 65.5 km altitude on Venus. At the start of the simulation only mode 1 contains droplets and mode 2 acquires droplets through mode-merging.

Table 7. Atmospheric conditions (from the VIRA profile at latitudes 0-30°) and initial parameters of the particle size distribution at 55 km altitude used in the coagulation test. The mode 1 initialization parameters are the standard deviation σ_1, the median radius r_{p1} and the total particle concentration N_{tot1}.

Parameter	**Value**
Altitude	55 km
Temperature	302.3 K
Pressure	$53.1 \cdot 10^3$ Pa
σ_1	1.56
r_{p1}	$3 \cdot 10^{-7}$ m
N_{tot1}	$2 \cdot 10^8$ m^{-3}

increase of the particle number M_0. Since the total particle concentration of mode 1 is much larger than that of mode 2, its decrease is much less visible in Fig. 11. The growth-related behavior seen in both Figures 11 and 13 is very similar to what was seen in Figures 8 and 9 for the mass transfer.

4. Conclusions

We have developed a modal microphysical model, MAD-VenLA, for modeling the clouds of Venus. The equations governing the microphysical processes of mass transfer and Brownian coagulation have been derived in the form necessary for the application of the moment method, basis of a modal microphysical model. This paper presents the derivations of the equations for all required flow regimes (continuum, transition, kinetic) and reports the hypotheses and estimation of parameters that were necessary in the development of the model. We have also included in the model the so-called mode-merging technique that allows the transfer of particles from one mode to another when modes overlap due to particle growth or decay. Such a technique is necessary when modeling aerosol dynamics of a multimodal particle population with a modal model. The developed model processes have been tested in a number of cases in average tropical atmospheric conditions on Venus. All of the model processes behave as expected. Heterogeneous nucleation is more efficient than homogeneous nucleation, as predicted by theory. Mass transfer tests on a pre-existing droplet population show that the particle sizes evolve as expected as a function of sub- and supersaturated conditions. Droplets shrink in size due to evaporation in subsaturated conditions, and this happens at an accelerating rate, since the growth rate is inversely proportional to the size of the particle. The inverse is seen in supersaturated conditions and the final size of the droplets depends on the growth rate and on the amount of available condensable vapor. The combination of a growth process (condensation or coagulation) and mode-merging on a single mode produces two modes due to growth and subsequent transfer of particles from

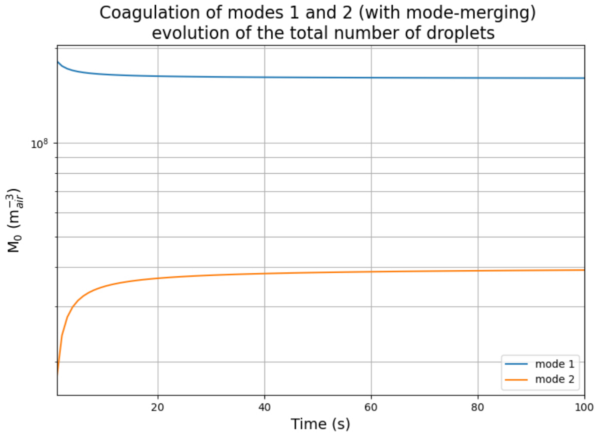

Fig. 11. Time evolution of the 0th order moment M_0 (total particle concentration) of modes 1 and 2 in the coagulation test with initial conditions as in Table 7.

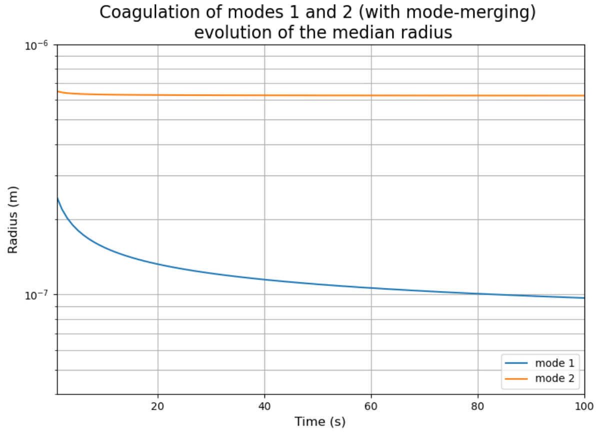

Fig. 12. Time evolution of the mode 1 and 2 median radii in the coagulation test with initial conditions as in Table 7.

the initial, smaller mode to a second, larger one. These tests provide the first validation of the proper functioning of the model. This model will be coupled with the IPSL Venus Global Climate Model in the near future to conduct simulations including transport, chemistry and cloud microphysics.

5. Acknowledgments

We acknowledge funding from the French national planetology program (PNP, Programme National de Planétologie) and the French Space Agency CNES. We are grateful for Aurélien Stozenbach and Slimane Bekki for their insight on sulfuric acid droplet properties and modeling and for Pascal Rannou on his expertise on aerosol modeling.

Appendix A. Detailed derivations of the microphysical processes used in the model

Appendix A.1. Heterogeneous nucleation

Appendix A.1.1. Calculation of the heterogeneous nucleation rate

As explained in Section 2.5, we use an effective heterogeneous nucleation rate calculated through a sectional parametrization. We tested two approaches, the first being to calculate the heterogeneous nucleation rate for pure sulfuric acid on a particle size

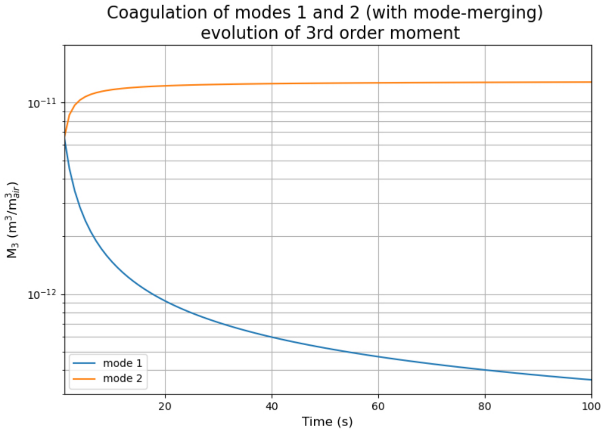

Fig. 13. Time evolution of the 3rd order moment M_0 (total particle volume) of modes 1 and 2 in the coagulation test with initial conditions as in Table 7.

distribution, and the second consists in calculating a simple activation of aerosols supposing that they correspond to acid solution droplets of the same size (approach also used by James et al. (1997)). We will describe the two parameterizations in the following.

The first approach is based on adapting a one-component nucleation routine (from the Mars global climate model, Navarro et al., 2014) to the nucleation of pure sulfuric acid. Calculating the nucleation rate for the median radius of the distribution only would lead to an instantaneous activation of all particles (supposed to have the same average radius), overestimating nucleation. To avoid this, we have divided the particle size distribution in several bins to calculate the heterogeneous nucleation rate J_{het}, allowing us to activate only a part of the distribution (above a certain size) as a function of the saturation ratio. We also had to estimate the values of certain parameters for sulfuric acid: the desorption energy, the energy for surface diffusion and the molecular vibration frequency. For these parameters we use the values for water (Montmessin et al., 2004). In addition, we also need to make a hypothesis on the contact parameter between the unknown aerosols and sulfuric acid. We use the value 0.946 that has been arbitrarily chosen as a compromise between numerical errors and number concentration of activated aerosols. The value is close to unity, meaning that we suppose the unknown aerosols to be easily wettable by sulfuric acid.

The second approach that accounts for the actual composition of the droplets is based on James et al. (1997). We predefine a size grid of unactivated aerosols and calculate, for each size bin, the saturation ratio supposing that the aerosol is a droplet of that size. The calculation accounts for the curvature and the thermodynamic conditions (temperature, vapor concentrations for H_2SO_4 and H_2O). When the saturation ratio for a certain size bin is larger than 1, the aerosols in this bin are activated as CN and become droplets of the same size. Otherwise ($S < 1$), the aerosols remain unactivated.

We have compared the two approaches for different size discretizations. The initial conditions of the tests are given in Table 4. The sum of activated aerosols gives the total number of CN.

One should note that the discretization has an effect on the precision on the fraction of activated aerosols, the result being better for a finer size grid. This can be seen in Fig. A.14 that shows as a function of the number of size bins the ratio of the calculated activated fraction and the reference given by the calculation using 10^6 bins. When the ratio is close to one, the result of the calculation using fewer bins approaches the result of the calculation using 10^6 bins, considered sufficiently accurate. However, the computational cost of such a high-resolution discretization can be prohibitive for applications in 3D atmospheric models. We have thus aimed at finding a compromise between the number of size bins and the accuracy of the result.

It can be seen that the results approach (for both parametrizations) the reference value given by the ideal case when the number of size bins is around 100, giving the order of magnitude of the required discretization for our model. As the approach of James et al. (1997) has the smallest difference compared to the reference even below 100 size bins and since it is computationally very efficient, we decided to opt for this routine for our model.

The total number of activated CN summed over the size grid gives the tendency of moment M_0 and the moment M_3 can be easily calculated from the bin radii and the number of activated CN in each bin summed over the size distribution.

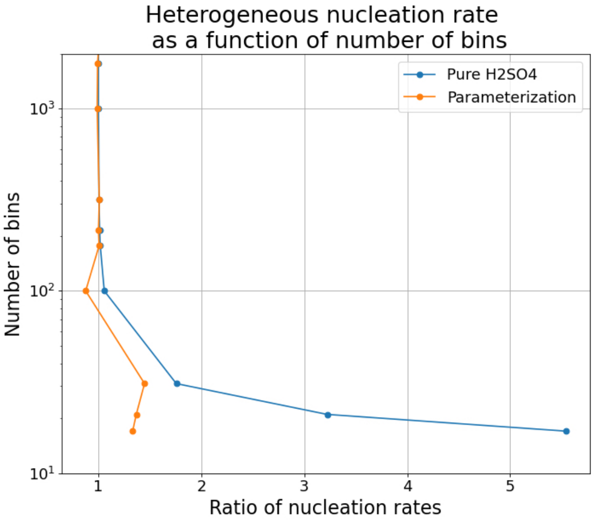

Fig. A.14. The ratio of the nucleation rate calculated with the parametrizations using different discretizations (number of bins given by the y-axis) and the "accurate" rate calculated with 10^6 bins. Orange line: approach of James et al. (1997); blue line: one-component nucleation of pure sulfuric acid.

Appendix A.2. Coagulation

Appendix A.2.1. Derivation and values of the b_k coefficients in the molecular regime

The calculation of the coefficients b_k (see Section 2.7, Eq. (48)) requires expressing the integrals of the coagulation equations (Equations (38)-(40)) with the functions $G(r_i, r_j, k)$ that represent the gain/loss of each mode, so that

$$I = \int_0^\infty \int_0^\infty \beta(r_i, r_j) G(r_i, r_j, k) n(r_i) n'(r_j) dr_i dr_j \tag{A.1}$$

Here, concerning the molecular regime, we can rewrite Eq. (A.1) :

$$\begin{aligned} I &= \int_0^\infty \int_0^\infty \sqrt{\frac{6kT}{\rho_g}} (r_i + r_j)^2 b_k (r_i^{-3/2} + r_j^{-3/2}) \\ &\times G(r_i, r_j, k) n(r_i) n'(r_j) dr_i dr_j \end{aligned} \tag{A.2}$$

From these expressions (Equations (A.1) and (A.2)) we get for b_k:

$$b_k = \frac{\int_0^\infty \int_0^\infty \beta(r_i, r_j) G(r_i, r_j, k) n(r_i) n'(r_j) dr_i dr_j}{\int_0^\infty \int_0^\infty \beta(r_i, r_j) \frac{r_i^{-3/2} + r_j^{-3/2}}{\sqrt{r_i^{-3} + r_j^{-3}}} G(r_i, r_j, k) n(r_i) n'(r_j) dr_i dr_j} \tag{A.3}$$

Table A.8 compiles the different expressions for $G(r_i, r_j, k)$ and b_k for the inter- and intra-modal interactions and modes.

Here we can see that there is a similarity: $b_3^{T2} \sim -b_3^{T4}$. This means that in inter-modal coagulation the loss of volume in mode 1 is equal to the gain in volume in mode 2. Certain coefficients are equal to zero ($b_3^{T1} \sim b_3^{T3} \sim b_0^{T4} \sim 0$) and there is thus no loss nor

Table A.8. Coefficients b_k and values of $G(r_i, r_j, k)$ for the moments of order k for modes 1 and 2. The last column (type) gives the type of interaction with (1-1) and (2-2) referring to intra-modal and ((1-2) to inter-modal coagulation.

Mode	b_k	$G(r_i, r_j, k)$	$G(k=0)$	$G(k=3)$	Type
1	b_k^{T1}	$(r_i^3+r_j^3)^{\frac{k}{3}} - r_i^k - r_j^k$	-1	0	(1-1)
1	b_k^{T2}	$-r_i^k$	-1	$-r_i^3$	(1-2)
2	b_k^{T3}	$(r_i^3+r_j^3)^{\frac{k}{3}} - r_i^k - r_j^k$	-1	0	(2-2)
2	b_k^{T4}	$(r_i^3+r_j^3)^{\frac{k}{3}} - r_j^k$	0	r_i^3	(1-2)

gain for the respective modes. These aspects reduce the number of coefficients b_k necessary for the calculations to four, and they are defined below.

$$b_0^{T1} = \frac{\int_0^\infty \int_0^\infty \beta_{11}(r_i, r_j) n_1(r_i) n_1(r_j) dr_i dr_j}{\int_0^\infty \int_0^\infty \beta_{11}(r_i, r_j) \frac{r_i^{-3/2}+r_j^{-3/2}}{\sqrt{r_i^{-3}+r_j^{-3}}} n_1(r_i) n_1(r_j) dr_i dr_j} \tag{A.4}$$

$$b_0^{T2} = \frac{\int_0^\infty \int_0^\infty \beta_{12}(r_i, r_j) n_1(r_i) n_2(r_j) dr_i dr_j}{\int_0^\infty \int_0^\infty \beta_{12}(r_i, r_j) \frac{r_i^{-3/2}+r_j^{-3/2}}{\sqrt{r_i^{-3}+r_j^{-3}}} n_1(r_i) n_2(r_j) dr_i dr_j} \tag{A.5}$$

$$b_3^{T2} = \frac{\int_0^\infty \int_0^\infty \beta_{12}(r_i, r_j) r_i^3 n_1(r_i) n_2(r_j) dr_i dr_j}{\int_0^\infty \int_0^\infty \beta_{12}(r_i, r_j) \frac{r_i^{3/2}+r_i^3 r_j^{-3/2}}{\sqrt{r_i^{-3}+r_j^{-3}}} n_1(r_i) n_2(r_j) dr_i dr_j} \tag{A.6}$$

$$b_0^{T3} = \frac{\int_0^\infty \int_0^\infty \beta_{22}(r_i, r_j) n_2(r_i) n_2(r_j) dr_i dr_j}{\int_0^\infty \int_0^\infty \beta_{22}(r_i, r_j) \frac{r_i^{-3/2}+r_j^{-3/2}}{\sqrt{r_i^{-3}+r_j^{-3}}} n_2(r_i) n_2(r_j) dr_i dr_j} \tag{A.7}$$

We have done the calculations for determining the values of b_k using Equations (A.4)-(A.7) as a function of droplet size in the ranges [1.0·10^{-9}, 5.5·10^{-7}] m for mode 1 and [5.45·10^{-7}, 2.0·10^{-5}] m for mode 2 (Fig. A.15). For the intra-modal interactions the value of b_0^{T1} is a constant as it only depends on the mode 1 radius range and is equal to 0.73, and similarly, $b_0^{T3} = 0.77$.

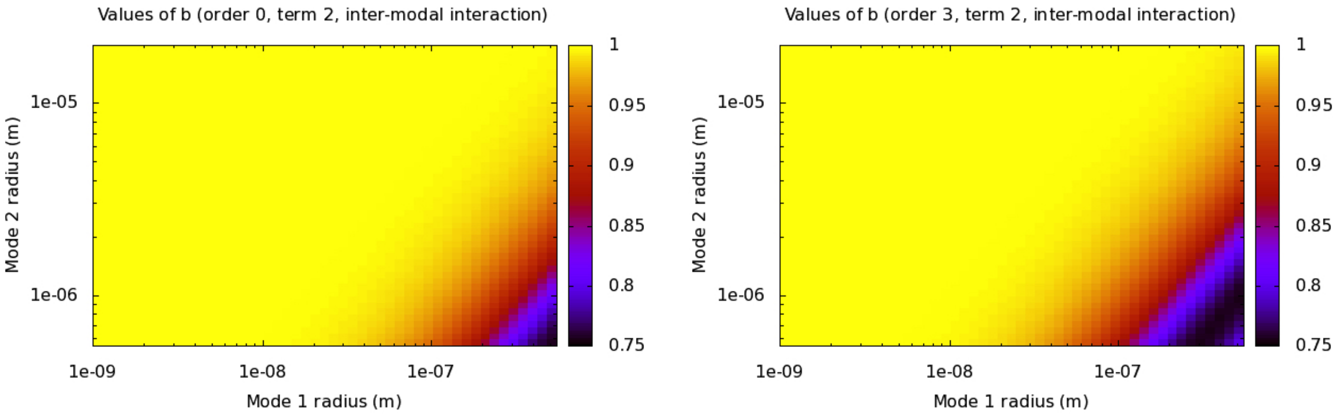

Fig. A.15. Values of b^{T2} for the 0th order moment (top) and 3rd order moment (bottom) for inter-modal interactions. The axes give the radii of the two modes. The black lines give the median radii of the two modes.

The results for b_0^{T2} and b_3^{T2} are shown in Figure A.15 that shows their dependence on the radii of modes 1 and 2. As the online calculation of these parameters is time-consuming, we have decided to use constant values for b_0^{T2} and b_3^{T2}. As we are using the moment method that considers the median radius of each mode, we have selected the b_k values corresponding to the median radii observed by Pioneer Venus, 300 nm for mode 1 and 1 μm for mode 2, that result in $b_0^{T2} = 0.88$ and $b_3^{T2} = 0.80$. We can see from Fig. A.15 that within the defined radius range the dominating value for b_0^{T2} and b_3^{T2} is 1.0. For the inter-modal interactions in a purely molecular regime, the choice of the values chosen above could lead to a maximum error of 15 % for b_0^{T2} and 20 % for b_3^{T2} compared to the value of unity. This might make a difference at the Venus cloud tops where homogeneously nucleated 1 nm droplets would be in this regime. However, since in our model we consider heterogeneous nucleation on CN with a mean radius of about 125 nm, the chosen values correspond quite well to the model regime.

Appendix A.2.2. Derivation of the moment M_0 and M_3 tendencies for modes 1 and 2 as a function of the flow regime

Table A.9 lists the tendencies of 0th and 3rd order moments for modes 1 and 2 as a function of the flow regime. The coefficients involved in the equations are given in Table A.10.

Table A.9. Equations for modes 1 et 2 for the two flow regimes and for the 0th and 3rd order moments. The coefficients $\gamma^{mode}_{order,regime}$ are derived in Appendix A.2.2 and are given in Table A.10.

Regime	**M$_k$**	**Mode**	**Expression**
CO	M$_0$	m1	$\frac{dM_0^{m1}}{dt} = \gamma_{0,CO}^{1A_{01}}(M_0^{m1})^2 + \gamma_{0,CO}^{1B_{01}} M_0^{m1} M_0^{m2}$
		m2	$\frac{dM_0^{m2}}{dt} = \gamma_{0,CO}^{2}(M_0^{m2})^2$
CO	M$_3$	m1	$\frac{dM_3^{m1}}{dt} = -\gamma_{3,CO}^{1} M_3^{m1} M_3^{m2}$
		m2	$\frac{dM_3^{m2}}{dt} = -\frac{dM_3^{m1}}{dt} = \gamma_{3,CO}^{1} M_3^{m1} M_3^{m2}$
FM	M$_0$	m1	$\frac{dM_0^{m1}}{dt} = \gamma_{0,FM}^{1A_{01}}(M_0^{m1})^2 + \gamma_{0,FM}^{1B_{01}} M_0^{m1} M_0^{m2}$
		m2	$\frac{dM_0^{m2}}{dt} = \gamma_{0,FM}^{2}(M_0^{m2})^2$
FM	M$_3$	m1	$\frac{dM_3^{m1}}{dt} = -\gamma_{3,FM} M_3^{m1} M_3^{m2}$
		m2	$\frac{dM_3^{m2}}{dt} = -\frac{dM_3^{m1}}{dt} = \gamma_{3,FM} M_3^{m1} M_3^{m2}$

Starting from equations (42) et (43) (Section 2.7), we can determine the 0th and 3rd order moment tendencies for mode 1 ($m1$) and mode 2 ($m2$) in the different flow regimes. For the 0th order moment of the two modes we get

$$\begin{aligned}\frac{dM_0^{m1}}{dt} &= -\frac{1}{2}\int_0^\infty \int_0^\infty \beta_{11}(r_i, r_j) n_1(r_i) n_1(r_j) dr_i dr_j \\ &\quad - \int_0^\infty \int_0^\infty \beta_{12}(r_i, r_j) n_1(r_i) n_2(r_j) dr_i dr_j \end{aligned} \tag{A.8}$$

$$\frac{dM_0^{m2}}{dt} = -\frac{1}{2}\int_0^\infty \int_0^\infty \beta_{22}(r_i, r_j) n_2(r_i) n_2(r_j) dr_i dr_j. \tag{A.9}$$

We will write the mode 1 equation (A.8) with two terms

$$\frac{dM_0^{m1}}{dt} = A_{01} + B_{01}. \tag{A.10}$$

Similarly, we will write the 3rd order moment for the two modes:

$$\frac{dM_3^{m1}}{dt} = \int_0^\infty \int_0^\infty \beta_{12}(r_i, r_j)(-r_i^3) n_1(r_i) n_2(r_j) dr_i dr_j \tag{A.11}$$

$$\frac{dM_3^{m2}}{dt} = \int_0^\infty \int_0^\infty \beta_{12}(r_i, r_j) r_i^3 n_1(r_i) n_2(r_j) dr_i dr_j \tag{A.12}$$

Inter-modal coagulation will make mode 1 lose volume that will be acquired by mode 2. This is why we can write:

$$\frac{dM_3^{m2}}{dt} = -\frac{dM_3^{m1}}{dt} \tag{A.13}$$

Table A.10. The coefficients $\gamma^{mode}_{order,regime}$ that appear in the equations of Table A.9.

Expression
$\gamma^{1A_{01}}_{0,CO} = -K_{CO}\left[1 + \alpha_1(1)\alpha_1(-1) + \bar{r}_1^{-1}C\left(\alpha_1(-1) + \alpha_1(-2)\alpha_1(1)\right)\right]$
$\gamma^{1B_{01}}_{0,CO} = -K_{CO}\Big[2 + \bar{r}_1\bar{r}_2^{-1}\alpha_1(1)\alpha_2(-1) + \bar{r}_1^{-1}\bar{r}_2\alpha_1(-1)\alpha_2(1)$ $+C\Big(\bar{r}_1^{-1}\alpha_1(-1) + \bar{r}_2^{-1}\alpha_2(-1) +$ $\bar{r}_1\bar{r}_2^{-2}\alpha_1(1)\alpha_2(-2) + \bar{r}_1^{-2}\bar{r}_2\alpha_1(-2)\alpha_2(1)\Big)\Big]$
$\gamma^{2}_{0,CO} = -K_{CO}\left[1 + \alpha_2(1)\alpha_2(-1) + \bar{r}_2^{-1}C\left(\alpha_2(-1) + \alpha_2(-2)\alpha_2(1)\right)\right]$
$\gamma^{1}_{3,CO} = -K_{CO}\Big[2\bar{r}_2^{-3}\frac{1}{\alpha_2(3)} + \bar{r}_1\bar{r}_2^{-4}\frac{\alpha_1(4)\alpha_2(-1)}{\alpha_1(3)\alpha_2(3)} + \bar{r}_1^{-1}\bar{r}_2^{-2}\frac{\alpha_1(2)\alpha_2(1)}{\alpha_1(3)\alpha_2(3)} +$ $C\Big(\bar{r}_1^{-1}\bar{r}_2^{-3}\frac{\alpha_1(2)}{\alpha_1(3)\alpha_2(3)} + \bar{r}_1\bar{r}_2^{-5}\frac{\alpha_1(4)\alpha_2(-2)}{\alpha_1(3)\alpha_2(3)} + \bar{r}_1^{-2}\bar{r}_2^{-2}\frac{\alpha_1(1)\alpha_2(1)}{\alpha_1(3)\alpha_2(3)} + \bar{r}_2^{-4}\frac{\alpha_2(-1)}{\alpha_2(3)}\Big)\Big]$
$\gamma^{1A_{01}}_{0,FM} = -b_0^{T1}K_{FM}r_1^{\frac{1}{2}}\left(\alpha_1(\tfrac{1}{2}) + \alpha_1(2)\alpha_1(-\tfrac{3}{2}) + \alpha_1(1)\alpha_1(-\tfrac{1}{2})\right)$
$\gamma^{1B_{01}}_{0,FM} = -b_0^{T2}K_{FM}\Big(\bar{r}_1^{\frac{1}{2}}\alpha_1(\tfrac{1}{2}) + \bar{r}_2^{\frac{1}{2}}\alpha_2(\tfrac{1}{2}) + 2\bar{r}_1^{-\frac{1}{2}}\bar{r}_2\alpha_1(-\tfrac{1}{2})\alpha_2(1)$ $+2\bar{r}_1\bar{r}_2^{-\frac{1}{2}}\alpha_1(1)\alpha_2(-\tfrac{1}{2})$ $+\bar{r}_1^2\bar{r}_2^{-\frac{3}{2}}\alpha_1(2)\alpha_2(-\tfrac{3}{2}) + \bar{r}_1^{-\frac{3}{2}}\bar{r}_2^2\alpha_1(-\tfrac{3}{2})\alpha_2(2)\Big)$
$\gamma^{2}_{0,FM} = -2b_0^{T1}K_{FM}r_2^{\frac{1}{2}}\left(\alpha_2(\tfrac{1}{2}) + \alpha_2(2)\alpha_2(-\tfrac{3}{2}) + \alpha_2(1)\alpha_2(-\tfrac{1}{2})\right)$
$\gamma_{3,FM} = b_3^{T2}K_{FM}\Big(\frac{r_1^{-\frac{5}{2}}}{r_2^3}\frac{\alpha_1(\frac{1}{2})}{\alpha_1(3)\alpha_2(3)} + \frac{r_1^{-1}}{r_2^{\frac{9}{2}}}\frac{\alpha_1(2)\alpha_2(-\frac{3}{2})}{\alpha_1(3)\alpha_2(3)}$ $+\frac{r_1^{-\frac{9}{2}}}{r_2}\frac{\alpha_1(-\frac{3}{2})\alpha_2(2)}{\alpha_1(3)\alpha_2(3)} + \frac{r_1^{-3}}{r_2^{\frac{5}{2}}}\frac{\alpha_2(\frac{1}{2})}{\alpha_1(3)\alpha_2(3)}$ $+2\frac{r_1^{-\frac{7}{2}}}{r_2^2}\frac{\alpha_1(-\frac{1}{2})\alpha_2(1)}{\alpha_1(3)\alpha_2(3)} + 2\frac{r_1^{-2}}{r_2^{\frac{7}{2}}}\frac{\alpha_1(1)\alpha_2(\frac{1}{2})}{\alpha_1(3)\alpha_2(3)}\Big)$

Appendix A.2.3. Moment M_0 and M_3 tendencies in the continuum regime

We write the intra-modal term A_{01} in Eq. (A.8) with β for continuum regime (Eq. (46)). We end up with an expression in powers of r:

$$\begin{aligned} A_{01} \;&=\; -\frac{1}{2}\int_0^\infty\int_0^\infty K_{CO}\Big[2 + \frac{r_i}{r_j} + \frac{r_j}{r_i} \\ &\quad +C\Big(\frac{1}{r_i} + \frac{1}{r_j} + \frac{r_i}{r_j^2} + \frac{r_j}{r_i^2}\Big)\Big]n_1(r_i)n_1(r_j)dr_idr_j. \end{aligned} \tag{A.14}$$

With Eq. (1) we can use the moments to rewrite:

$$\begin{aligned} A_{01} \;&=\; -\frac{1}{2}K_{CO}\Big[2M_0^{m1}M_0^{m1} + M_1^{m1}M_{-1}^{m1} + M_{-1}^{m1}M_1^{m1} \\ &\quad +C\Big(M_{-1}^{m1}M_0^{m1} + M_0^{m1}M_{-1}^{m1} \\ &\quad +M_1^{m1}M_{-2}^{m1} + M_{-2}^{m1}M_1^{m1}\Big)\Big]. \end{aligned} \tag{A.15}$$

With the help of Eq. (3) we can replace the moments of order $k \neq 0$ by the 0th order moments. As we are only using 0th and 3rd order moments in the model, we can write

$$A_{01} \;=\; -K_{CO}\Big[1 + \alpha_1(1)\alpha_1(-1)$$

$$
\begin{aligned}
&+\bar{r}_1^{-1}C\Big(\alpha_1(-1)+\alpha_1(-2)\alpha_1(1)\Big)\Big](M_0^{m1})^2\\
= \;& \gamma_{0,CO}^{1A_{01}}(M_0^{m1})^2. \qquad \text{(A.16)}
\end{aligned}
$$

This term describes the intra-modal interactions of mode 1. Coagulation induces a loss in the number concentration of mode 1, so $A_{01} < 0$.

Then we proceed in the same way to write the inter-modal term for mode 1 (Eq. (A.8)) that we note B_{01}:

$$
\begin{aligned}
B_{01} &= -\int_0^\infty\int_0^\infty K_{CO}\Big[2+\frac{r_i}{r_j}+\frac{r_j}{r_i}\\
&\quad +C\Big(\frac{1}{r_i}+\frac{1}{r_j}+\frac{r_i}{r_j^2}+\frac{r_j}{r_i^2}\Big)\Big]n_1(r_i)n_2(r_j)dr_idr_j\\
&= -K_{CO}\Big[2M_0^{m1}M_0^{m2}+M_1^{m1}M_{-1}^{m2}+M_{-1}^{m1}M_1^{m2}\\
&\quad +C\Big(M_{-1}^{m1}M_0^{m2}+M_1^{m1}M_{-2}^{m2}+M_{-2}^{m1}M_1^{m2}+M_0^{m1}M_{-1}^{m2}\Big)\Big]\\
&= -K_{CO}\Big[2+\bar{r}_1\bar{r}_2^{-1}\alpha_1(1)\alpha_2(-1)+\bar{r}_1^{-1}\bar{r}_2\alpha_1(-1)\alpha_2(1)\\
&\quad +C\Big(\bar{r}_1^{-1}\alpha_1(-1)+\bar{r}_2^{-1}\alpha_2(-1)+\bar{r}_1\bar{r}_2^{-2}\alpha_1(1)\alpha_2(-2)\\
&\quad +\bar{r}_1^{-2}\bar{r}_2\alpha_1(-2)\alpha_2(1)\Big)\Big]\cdot M_0^{m1}M_0^{m2}\\
&= \gamma_{0,CO}^{1B_{01}}M_0^{m1}M_0^{m2} \qquad \text{(A.17)}
\end{aligned}
$$

The term B_{01} gives the loss of droplets in mode 1 and gain in mode 2 due to inter-modal coagulation. This is why B_{01} depends both on M_0^{m1} and M_0^{m2}. Now we rewrite Eq. (A.10) and insert in A_{01} (Eq. (A.16)) and B_{01} (Eq. (A.17)) with the constants $\gamma_{0,CO}^{1A_{01}}$ and $\gamma_{0,CO}^{1B_{01}}$, giving the following expression for mode 1:

$$
\frac{dM_0^{m1}}{dt}=\gamma_{0,CO}^{1A_{01}}(M_0^{m1})^2+\gamma_{0,CO}^{1B_{01}}M_0^{m1}M_0^{m2}. \qquad \text{(A.18)}
$$

For mode 2 we get:

$$
\begin{aligned}
\frac{dM_0^{m2}}{dt} &= -K_{CO}\Big[1+\alpha_2(1)\alpha_2(-1)\\
&\quad +\bar{r}_2^{-1}C\Big(\alpha_2(-1)+\alpha_2(-2)\alpha_2(1)\Big)\Big](M_0^{m2})^2. \qquad \text{(A.19)}
\end{aligned}
$$

This can also be written as follows:

$$
\frac{dM_0^{m2}}{dt}=\gamma_{0,CO}^{2}(M_0^{m2})^2. \qquad \text{(A.20)}
$$

We use the same approach to define the tendency of the 3rd order moment for mode 1 and consequently deduce the tendency for mode 2, starting from Equations (46) and (A.9):

$$
\begin{aligned}
\frac{dM_3^{m1}}{dt} &= \int_0^\infty\int_0^\infty K_{CO}\Big[2+\frac{r_i}{r_j}+\frac{r_j}{r_i}\\
&\quad +C\Big(\frac{1}{r_i}+\frac{1}{r_j}+\frac{r_i}{r_j^2}+\frac{r_j}{r_i^2}\Big)\Big](-r_i^3)n_1(r_i)n_1(r_j)dr_idr_j\\
&= -K_{CO}\Big[2M_3^{m1}M_0^{m2}+M_4^{m1}M_{-1}^{m2}+M_2^{m1}M_1^{m2}
\end{aligned}
$$

$$\begin{aligned}
& +C\Big(M_2^{m1}M_0^{m2} + M_4^{m1}M_{-2}^{m2} + M_1^{m1}M_1^{m2} + M_3^{m1}M_{-1}^{m2}\Big)\Big] \\
= \;& -K_{CO}\Big[2\bar{r}_2^{-3}\frac{1}{\alpha_2(3)} + \bar{r}_1\bar{r}_2^{-4}\frac{\alpha_1(4)\alpha_2(-1)}{\alpha_1(3)\alpha_2(3)} \\
& +\bar{r}_1^{-1}\bar{r}_2^{-2}\frac{\alpha_1(2)\alpha_2(1)}{\alpha_1(3)\alpha_2(3)} + C\Big(\bar{r}_1^{-1}\bar{r}_2^{-3}\frac{\alpha_1(2)}{\alpha_1(3)\alpha_2(3)} \\
& +\bar{r}_1\bar{r}_2^{-5}\frac{\alpha_1(4)\alpha_2(-2)}{\alpha_1(3)\alpha_2(3)} + \bar{r}_1^{-2}\bar{r}_2^{-2}\frac{\alpha_1(1)\alpha_2(1)}{\alpha_1(3)\alpha_2(3)} \\
& +\bar{r}_2^{-4}\frac{\alpha_2(-1)}{\alpha_2(3)}\Big)\Big]M_3^{m1}M_3^{m2} \\
= \;& \gamma^1_{3,CO}M_3^{m1}M_3^{m2}.
\end{aligned} \tag{A.21}$$

Thus the tendencies are:

$$\frac{dM_3^{m2}}{dt} = -\frac{dM_3^{m1}}{dt} = -\gamma^1_{3,CO}M_3^{m1}M_3^{m2} \tag{A.22}$$

This equation shows that the volume lost in mode 1 through inter-modal coagulation is a gain for mode 2.

Appendix A.2.4. Moment M_0 and M_3 tendencies in the molecular regime

Just like for the continuum regime the equations for modes 1 and 2 depend on the Eq. (48) of the coagulation coefficient for the molecular regime. Thus we will need the Equations (A.9), (A.12) and (A.14) for expressing the tendencies of the 0th and 3rd order moments in this regime.

Let us start with the 0th order moment. For mode 1 we will derive separately the terms A_{01} (Eq. (A.14)) and B_{01} (Eq. (A.17)):

$$\begin{aligned}
A_{01} \;=\;& -\int_0^\infty\int_0^\infty \beta_{FM}(r_i,r_j)n_1(r_i)n_1(r_j)dr_idr_j \\
=\;& -\int_0^\infty\int_0^\infty b_0^{T1}\beta_{1\leftrightarrow 2}(r_i,r_j)n_1(r_i)n_1(r_j)dr_idr_j \\
=\;& -b_0^{T1}K_{FM}r_1^{\frac{1}{2}}\Big(\alpha_1(\frac{1}{2}) + \alpha_1(2)\alpha_1(-\frac{3}{2}) \\
& +\alpha_1(1)\alpha_1(-\frac{1}{2})\Big)(M_0^{m1})^2 \\
=\;& \gamma^{1A_{01}}_{0,FM}(M_0^{m1})^2,
\end{aligned} \tag{A.23}$$

$$\begin{aligned}
B_{01} \;=\;& -\int_0^\infty\int_0^\infty \beta_{FM}(r_i,r_j)n_1(r_i)n_2(r_j)dr_idr_j \\
=\;& -\int_0^\infty\int_0^\infty b_0^{T2}\beta_{1\leftrightarrow 2}(r_i,r_j)n_1(r_i)n_2(r_j)dr_idr_j \\
=\;& -b_0^{T2}K_{FM}\Big(M_{\frac{1}{2}}^{m1}M_0^{m2} + M_0^{m1}M_{\frac{1}{2}}^{m2} + 2M_{-\frac{1}{2}}^{m1}M_1^{m2} \\
& +2M_1^{m1}M_{-\frac{1}{2}}^{m2} + M_2^{m1}M_{-\frac{3}{2}}^{m2} + M_{-\frac{3}{2}}^{m1}M_2^{m2}\Big) \\
=\;& -b_0^{T2}K_{FM}\Big(\bar{r}_1^{\frac{1}{2}}\alpha_1(\frac{1}{2}) + \bar{r}_2^{\frac{1}{2}}\alpha_2(\frac{1}{2}) \\
& +2\bar{r}_1^{-\frac{1}{2}}\bar{r}_2\alpha_1(-\frac{1}{2})\alpha_2(1) + 2\bar{r}_1\bar{r}_2^{-\frac{1}{2}}\alpha_1(1)\alpha_2(-\frac{1}{2}) \\
& +\bar{r}_1^2\bar{r}_2^{-\frac{3}{2}}\alpha_1(2)\alpha_2(-\frac{3}{2}) + \bar{r}_1^{-\frac{3}{2}}\bar{r}_2^2\alpha_1(-\frac{3}{2})\alpha_2(2)\Big) \\
& \times M_0^{m1}M_0^{m2} \\
=\;& \gamma^{1B_{01}}_{0,FM}M_0^{m1}M_0^{m2}.
\end{aligned} \tag{A.24}$$

Using the constants $\gamma^{1A_{01}}_{0,FM}$ and $\gamma^{1A_{01}}_{0,FM}$ in A_{01} (Eq. (A.23)) and B_{01} (Eq. (A.24)), we get:

$$\frac{dM^{m1}_0}{dt} = \gamma^{1A_{01}}_{0,FM}(M^1_0)^2 + \gamma^{1B_{01}}_{0,FM} M^{m1}_0 M^{m2}_0 \tag{A.25}$$

and

$$\begin{aligned}\frac{dM^{m2}_0}{dt} \quad &= -2b^{T1}_0 K_{FM} r_2^{\frac{1}{2}}\Bigg(\alpha_2(\frac{1}{2}) + \alpha_2(2)\alpha_2(-\frac{3}{2}) \\ &+\alpha_2(1)\alpha_2(-\frac{1}{2})\Bigg)(M^{m2}_0)^2\end{aligned} \tag{A.26}$$

giving

$$\frac{dM^{m2}_0}{dt} = \gamma^2_{0,FM}(M^{m2}_0)^2 \tag{A.27}$$

For the 3$^{\text{rd}}$ order moments we acquire in a similar fashion:

$$\begin{aligned}\frac{dM^{m1}_3}{dt} \quad &= \int_0^\infty \int_0^\infty \beta_{FM}(r_i, r_j) n_1(r_i) n_2(r_j) dr_i dr_j \\ &= \int_0^\infty \int_0^\infty b^{T2}_3 \beta_{1\leftrightarrow 2}(r_i, r_j) n_1(r_i) n_2(r_j) dr_i dr_j \\ &= b^{T2}_3 K_{FM}\Bigg(M^{m1}_{\frac{1}{2}} M^{m2}_0 + M^{m1}_2 M^{m2}_{-\frac{3}{2}} + M^{m1}_{-\frac{3}{2}} M^{m2}_2 \\ &+M^{m1}_0 M^{m2}_{\frac{1}{2}} + 2M^{m1}_{-\frac{1}{2}} M^{m2}_1 + 2M^{m1}_1 M^{m2}_{-\frac{1}{2}}\Bigg)\end{aligned} \tag{A.28}$$

and

$$\begin{aligned}\frac{dM^{m1}_3}{dt} \quad &= b^{T2}_3 K_{FM}\Bigg(\frac{r_1^{-\frac{5}{2}}}{r_2^3}\frac{\alpha_1(\frac{1}{2})}{\alpha_1(3)\alpha_2(3)} + \frac{r_1^{-1}}{r_2^{\frac{9}{2}}}\frac{\alpha_1(2)\alpha_2(-\frac{3}{2})}{\alpha_1(3)\alpha_2(3)} \\ &+\frac{r_1^{-\frac{9}{2}}}{r_2}\frac{\alpha_1(-\frac{3}{2})\alpha_2(2)}{\alpha_1(3)\alpha_2(3)} + \frac{r_1^{-3}}{r_2^{\frac{5}{2}}}\frac{\alpha_2(\frac{1}{2})}{\alpha_1(3)\alpha_2(3)} \\ &+2\frac{r_1^{-\frac{7}{2}}}{r_2^2}\frac{\alpha_1(-\frac{1}{2})\alpha_2(1)}{\alpha_1(3)\alpha_2(3)} + 2\frac{r_1^{-2}}{r_2^{\frac{7}{2}}}\frac{\alpha_1(1)\alpha_2(\frac{1}{2})}{\alpha_1(3)\alpha_2(3)}\Bigg) \\ &\times M^{m1}_3 M^{m2}_3\end{aligned} \tag{A.29}$$

giving

$$\frac{dM^{m1}_3}{dt} = \gamma_{3,FM} M^{m1}_3 M^{m2}_3 = -\frac{dM^{m2}_3}{dt}. \tag{A.30}$$

In the molecular regime the coagulation tendencies for inter- and intra-modal interactions follow the same logic as for the continuum regime. For intra-modal coagulation, the total volume is conserved, and the volume lost by mode 1 is transferred to mode 2.

Appendix A.2.5. Explicit expressions for the coagulation tendencies

Now that we have at hand the expressions for calculating the variations of the moments for the two modes (Table A.9), we will be able to write them in an explicit form with the help of the coefficients γ (Table A.10).

$$\begin{aligned}M^{m1}_{0,t+1} \quad &= \quad \frac{1-\gamma^{1B}_0 \Delta t M^{m2}_{0,t+1}}{2\gamma^{1A}_0 \Delta t} \\ &\quad + \sqrt{\frac{M^{m1}_{0,t}}{\gamma^{1A}_0 \Delta t} - \left[\frac{1-\gamma^{1B}_0 \Delta t M^{m2}_{0,t+1}}{2\gamma^{1A}_0 \Delta t}\right]^2}\end{aligned} \tag{A.31}$$

$$M^{m2}_{0,t+1} \quad = \quad \frac{1}{2\gamma^2_0 \Delta t} + \sqrt{\frac{M^{m2}_{0,t}}{\gamma^2_0 \Delta t} - \frac{1}{4\gamma^2_0 \Delta t^2}} \tag{A.32}$$

Eq. (A.32) can be inserted in (A.31). For the 3rd order we get:

$$\begin{aligned}
M^{m1}_{3,t+1} &= \frac{-1}{2\gamma_3 \Delta t} - \frac{1}{2}(M^{m1}_{3,t} - M^{m2}_{3,t}) \\
&\quad + \sqrt{\frac{M^{m1}_{3,t}}{\gamma_3 \Delta t} + \frac{1}{4}\left[\frac{1}{\gamma_3 \Delta t} + (M^{m1}_{3,t} + M^{m2}_{3,t})\right]^2} \qquad \text{(A.33)} \\
M^{m2}_{3,t+1} &= \frac{1}{2\gamma_3 \Delta t} + \frac{1}{2}(M^{m2}_{3,t} - M^{m1}_{3,t}) \\
&\quad + \sqrt{-\frac{M^{m2}_{3,t}}{\gamma_3 \Delta t} + \frac{1}{4}\left[\frac{1}{\gamma_3 \Delta t} + (M^{m2}_{3,t} + M^{m1}_{3,t})\right]^2} \qquad \text{(A.34)}
\end{aligned}$$

With the adequate coefficients γ (Table A.10), these equations are valid for both the continuum and molecular regimes.

Appendix B. Processes included for cloud modeling in an atmospheric column

Appendix B.1. Aerosol production

The formation of clouds via heterogeneous nucleation requires the presence of solid aerosol particles that function as condensation nuclei. We do not know the composition of the possible CN in the atmosphere of Venus so this approach requires certain hypotheses. First of all, for the purpose of 1-3D modeling, we need to define their distribution as a function of altitude that we have chosen as follows:

$$\frac{dM_3}{dt} = \frac{\gamma_{aer}}{\frac{4}{3}\pi \rho_{aer} dz} \qquad \text{(B.1)}$$

where γ_{aer} is the production rate of aerosols in kg m^{-2} s^{-1} and ρ_{aer} the density of the aerosol particles. The parameter dz is the width (or standard deviation) of the gaussian distribution used for describing the aerosol layer. We apply the explicit scheme and write:

$$M_{3,t+1} = \frac{\gamma_{aer}}{\frac{4}{3}\pi \rho_{aer} dz} \Delta t + M_{3,t} \qquad \text{(B.2)}$$

The zeroth order moment is acquired by:

$$M_{0,t+1} = \frac{1}{r^3_{aer}\alpha_{aer}(3)} M_{3,t+1}. \qquad \text{(B.3)}$$

The produced aerosol particles are activated by heterogeneous nucleation to allow for the formation of droplets in the model that act as a sink for the aerosols. When the droplets evaporate, the aerosol particles are released.

Appendix B.2. Sedimentation

The model includes the possibility to calculate sedimentation in case it is used in a 1D setting. Although in this paper the model is only used in 0D, we present in the following the equations for calculating sedimentation with moments. For sedimentation we have applied the same approach as Burgalat (2012). We can write:

$$v_{\mathrm{t}}(r,z) = \frac{2}{9}\frac{r^2 \rho_{\mathrm{g}} g_0 (1 + A_{CM} K_n)}{\mu_{air}} \qquad \text{(B.4)}$$

allowing us to write the sedimentation flux F_{sed} as a function of powers of r:

$$F_{sed}(\Delta r, z) = \int_r^{r+dr} n(r,z) v_t(r,z) dr. \qquad \text{(B.5)}$$

If we replace v_t in Eq. (B.5) with Eq. (B.4), we obtain:

$$F_{sed}(\Delta r, z) = \int_{r}^{r+dr} n(r,z) \frac{2}{9} \frac{r^2 \rho_g g_0 (1 + A_{CM} K_n)}{\mu_{air}} dr \tag{B.6}$$

Expressing Eq. (B.6) with moments, we finally get:

$$F_{sed,M_k}(z) = \frac{2\rho_g g_0}{9\mu_{air}} (M_k^{k+2} + A_{CM} \lambda_g M_k) \tag{B.7}$$

The expression (B.7) allows us to determine the sedimentation flux in an atmospheric column (1D). Just like for coagulation, we use the approximation of the Cunningham-Millikan correction $A_{CM} = 1.591$ Park et al. (1999)). This produces an error very similar to that of the coagulation, from -4 to 9% (Burgalat, 2012).

References

Burgalat, J. (2012). *Développement d'un modèle microphysique en moments pour les modèles climatiques de Titan*. Ph.D. thesis Ecole doctorale Sciences, technologies, santé.

Burgalat, J., & Rannou, P. (2017). Brownian coagulation of a bi-modal distribution of both spherical and fractal aerosols. *J. Aerosol Sci.*, *105*, 151–165. URL: https://www.sciencedirect.com/science/article/pii/S0021850215300951. doi:https://doi.org/10.1016/j.jaerosci.2016.11.009.

Burgalat, J., Rannou, P., Cours, T., & Rivière, E. (2014). Modeling cloud microphysics using a two-moments hybrid bulk/bin scheme for use in titan's climate models: Application to the annual and diurnal cycles. *Icarus*, *231*, 310–322. URL: https://www.sciencedirect.com/science/article/pii/S0019103513005307. doi:https://doi.org/10.1016/j.icarus.2013.12.012.

Esposito, L. W., Bertaux, J. L., Krasnopolsky, V., Moroz, V. I., & Zasova, L. V. (1997). Chemistry of Lower Atmosphere and Clouds. In S. W. Bougher, D. M. Hunten, & R. J. Phillips (Eds.), *Venus II: Geology, Geophysics, Atmosphere, and Solar Wind Environment* (p. 415).

Esposito, L. W., Knollenberg, R. G., Marov, M. I., Toon, O. B., & Turco, R. P. (1983). The clouds and hazes of Venus. In *Venus* (pp. 484–564).

Friedlander, S. K. et al. (2000). *Smoke, dust, and haze*. Oxford university press.

Fuchs, N. A. (1964). *The mechanics of Aerosol*. New York: Pergamon.

Gao, P., Zhang, X., Crisp, D., Bardeen, C. G., & Yung, Y. L. (2014). Bimodal distribution of sulfuric acid aerosols in the upper haze of Venus. *Icarus*, *231*, 83–98. doi:10.1016/j.icarus.2013.10.013. arXiv:1312.3750.

Haberle, R. M., Kahre, M. A., Hollingsworth, J. L., Montmessin, F., Wilson, R. J., Urata, R. A., Brecht, A. S., Wolff, M. J., Kling, A. M., & Schaeffer, J. R. (2019). Documentation of the nasa/ames legacy mars global climate model: Simulations of the present seasonal water cycle. *Icarus*, *333*, 130–164. URL: https://www.sciencedirect.com/science/article/pii/S0019103518305761. doi:https://doi.org/10.1016/j.icarus.2019.03.026.

Hashimoto, G. L., & Abe, Y. (2001). Predictions of a simple cloud model for water vapor cloud albedo feedback on venus. *Journal of Geophysical Research: Planets*, *106*(E7), 14675–14690. URL: https://agupubs.onlinelibrary.wiley.com/doi/abs/10.1029/2000JE001266. doi:https://doi.org/10.1029/2000JE001266. arXiv:https://agupubs.onlinelibrary.wiley.com/doi/pdf/10.1029/2000JE001266.

Hunten, D. M., Turco, R. P., & Toon, O. B. (1980). Smoke and dust particles of meteoritic origin in the mesosphere and stratosphere. *J. Atmos. Sci.*, *37*, 1342.

Imamura, T., & Hashimoto, G. L. (1998). Venus cloud formation in the meridional circulation. *J. Geophys. Res.*, *103*, 31349–31366. doi:10.1029/1998JE900010.

Imamura, T., & Hashimoto, G. L. (2001). Microphysics of venusian clouds in rising tropical air. *Journal of the Atmospheric Sciences*, *58*(23), 3597 – 3612. URL: https://journals.ametsoc.org/view/journals/atsc/58/23/1520-0469_2001_058_3597_movcir_2.0.co_2.xml. doi:10.1175/1520-0469(2001)058<3597:MOVCIR>2.0.CO;2.

James, E. P., Toon, O. B., & Schubert, G. (1997). A numerical microphysical model of the condensational Venus cloud. *Icarus*, *129*, 147–171.

Kliore, A. J., Moroz, V. I., & Keating, G. M. (1985). The Venus International Reference Atmosphere. *Advances in Space Research*, *5*.

Knollenberg, R. G., & Hunten, D. M. (1980). The microphysics of the clouds of Venus - Results of the Pioneer Venus particle size spectrometer experiment. *J. Geophys. Res.*, *85*, 8039–8058. doi:10.1029/JA085iA13p08039.

Krasnopolsky, V., & Pollack, J. (1994). H2o-h2so4 system in venus' clouds and ocs, co, and h2so4 profiles in venus' troposphere. *Icarus*, *109*(1), 58–78. URL: https://www.sciencedirect.com/science/article/pii/S0019103584710773. doi:https://doi.org/10.1006/icar.1994.1077.

Kuroda, T. (1984). Rate determining processes of growth of ice crystals from the vapour phase. *Journal of the Meteorological Society of Japan. Ser. II*, *62*(3), 552–562. doi:10.2151/jmsj1965.62.3_552.

Lebonnois, S., Hourdin, F., Eymet, V., Crespin, A., Fournier, R., & Forget, F. (2010). Superrotation of Venus' atmosphere analyzed with a full general circulation model. *J. Geophys. Res.*, *115*, 6006. doi:10.1029/2009JE003458.

Lee, C., Lewis, S. R., & Read, P. L. (2010). A bulk cloud parameterization in a venus general circulation model. *Icarus*, *206*(2), 662–668. URL: https://www.sciencedirect.com/science/article/pii/S0019103509004114. doi:https://doi.org/10.1016/j.icarus.2009.09.017. Cassini at Saturn.

Lee, K. W., & Chen, H. (1984). Coagulation rate of polydisperse particles. *Aerosol Science and Technology*, *3*(3), 327–334. URL: https://doi.org/10.1080/02786828408959020. doi:10.1080/02786828408959020. arXiv:https://doi.org/10.1080/02786828408959020.

Limaye, S. S., Grassi, D., Mahieux, A., Migliorini, A., Tellmann, S., & Titov, D. (2018). Venus Atmospheric Thermal Structure and Radiative Balance. *Space Sci. Rev.*, *214*(5), 102. doi:10.1007/s11214-018-0525-2.

Määttänen, A., Mathé, C., Audouard, J., Listowski, C., Millour, E., Forget, F., González-Galindo, F., Falletti, L., Bardet, D., Teinturier, L., Vals, M., Spiga, A., & Montmessin, F. (2022). Troposphere-to-mesosphere microphysics of carbon dioxide ice clouds in a mars global climate model. *Icarus*, (p. 115098). URL: https://www.sciencedirect.com/science/article/pii/S0019103522002056. doi:https://doi.org/10.1016/j.icarus.2022.115098.

Määttänen, A., Merikanto, J., Henschel, H., Duplissy, J., Makkonen, R., Ortega, I. K., & Vehkamäki, H. (2018). New parameterizations for neutral and ion-induced sulfuric acid-water particle formation in nucleation and kinetic regimes. *Journal of Geophysical Research: Atmospheres*, *123*(2), 1269–1296. URL: https://agupubs.onlinelibrary.wiley.com/doi/abs/10.1002/2017JD027429. doi:https://doi.org/10.1002/2017JD027429.

Mann, G. W., Carslaw, K. S., Spracklen, D. V., Ridley, D. A., Manktelow, P. T., Chipperfield, M. P., Pickering, S. J., & Johnson, C. E. (2010). Description and evaluation of glomap-mode: a modal global aerosol microphysics model for the ukca composition-climate model. *Geoscientific Model Development*, *3*(2), 519–551. URL: https://gmd.copernicus.org/articles/3/519/2010/. doi:10.5194/gmd-3-519-2010.

Marcq, E., Mills, F. P., Parkinson, C. D., & Vandaele, A. C. (2018). Composition and Chemistry of the Neutral Atmosphere of Venus. *Space Sci. Rev.*, *214*(1), 10. doi:10.1007/s11214-017-0438-5.

McGouldrick, K., & Toon, O. B. (2007). An investigation of possible causes of the holes in the condensational Venus cloud using a microphysical cloud model with a radiative-dynamical feedback. *Icarus*, *191*, 1–24. doi:10.1016/j.icarus.2007.04.007.

Montmessin, F., Forget, F., Rannou, P., Cabane, M., & Haberle, R. M. (2004). Origin and role of water ice clouds in the Martian water cycle as inferred from a general circulation model. *J. Geophys. Res*, *109*, E10004.

Navarro, T., Madeleine, J.-B., Forget, F., Spiga, A., Millour, E., Montmessin, F., & Määttänen, A. (2014). Global Climate Modeling of the Martian water cycle with improved microphysics and radiatively active water ice clouds. *J. Geophys. Res.*, . doi:10.1002/2013JE004550.

Otto, E., Fissan, H., Park, S., & Lee, K. (1999). The log-normal size distribution theory of brownian aerosol coagulation for the entire particle size range: part ii—analytical solution using dahneke's coagulation kernel. *Journal of Aerosol Science*, *30*(1), 17–34. URL: https://www.sciencedirect.com/science/article/pii/S002185029800038X. doi:https://doi.org/10.1016/S0021-8502(98)00038-X.

Park, S., Lee, K., Otto, E., & Fissan, H. (1999). The log-normal size distribution theory of brownian aerosol coagulation for the entire particle size range: Part i—analytical solution using the harmonic mean coagulation kernel. *Journal of Aerosol Science*, *30*(1), 3–16. URL: https://www.sciencedirect.com/science/article/pii/S0021850298000378. doi:https://doi.org/10.1016/S0021-8502(98)00037-8.

Parkinson, C. D., Gao, P., Esposito, L., Yung, Y., Bougher, S., & Hirtzig, M. (2015a). Photochemical control of the distribution of Venusian water. *Planet. Space Sci.*, *113*, 226–236. doi:10.1016/j.pss.2015.02.015.

Parkinson, C. D., Gao, P., Schulte, R., Bougher, S. W., Yung, Y. L., Bardeen, C. G., Wilquet, V., Vandaele, A. C., Mahieux, A., Tellmann, S., & Pätzold, M. (2015b). Distribution of sulphuric acid aerosols in the clouds and upper haze of Venus using Venus Express VAST and VeRa temperature profiles. *Planet. Space Sci.*, *113*, 205–218. doi:10.1016/j.pss.2015.01.023.

Steele, H. M., & Hamill, P. (1981). Effects of temperature and humidity on the growth and optical properties of sulphuric acid—water droplets in the stratosphere. *Journal of aerosol science*, *12*(6), 517–528.

Stolzenbach, A. (2016). *Etude de la photochimie de Vénus à l'aide d'un modèle de circulation générale*. Ph.D. thesis École doctorale Sciences de l'environnement d'Île-de-France.

Titov, D. V., Ignatiev, N. I., McGouldrick, K., Wilquet, V., & Wilson, C. F. (2018). Clouds and Hazes of Venus. *Space Sci. Rev.*, *214*(8), 126. doi:10.1007/s11214-018-0552-z.

Toon, O. B., Turco, R. P., & Pollack, J. B. (1982). The ultraviolet absorber on venus: Amorphous sulfur. *Icarus*, *51*(2), 358–373. URL: https://www.sciencedirect.com/science/article/pii/0019103582900896. doi:https://doi.org/10.1016/0019-1035(82)90089-6.

Toon, O. B., Turco, R. P., Westphal, D., Malone, R., & Liu, M. (1988). A multidimensional model for aerosols: description of computational analogs. *J. Atm. Sci.*, *45*, 2123–2143.

Turco, R. P., Hamill, P., Toon, O. B., Whitten, R. C., & Kiang, C. S. (1979). A one-dimensional model describing aerosol formation and evolution in the stratosphere: I. physical processes and mathematical analogs. *Journal of the Atmospheric Sciences*, *36*, 699–717.

Vehkamäki, H., Kulmala, M., Lehtinen, K. E. J., & Noppel, M. (2003). Modeling binary homogeneous nucleation of water-sulfuric acid vapours: Parameterisation for high temperature emissions. *Environmental Science and Technology*, *37*(15), 3392–3398. URL: https://doi.org/10.1021/es0263442. doi:10.1021/es0263442.

Vehkamäki, H., Kulmala, M., Napari, I., Lehtinen, K. E. J., Timmreck, C., Noppel, M., & Laaksonen, A. (2002). An improved parameterization for sulfuric acid/water nucleation rates for tropospheric and stratospheric conditions. *J. Geophys. Res.*, *107*, 10.1029/2002JD00.

Vignati, E., Wilson, J., & Stier, P. (2004). M7: An efficient size-resolved aerosol microphysics module for large-scale aerosol transport models. *Journal of Geophysical Research: Atmospheres*, *109*(D22). URL: https://agupubs.onlinelibrary.wiley.com/doi/abs/10.1029/2003JD004485. doi:https://doi.org/10.1029/2003JD004485. arXiv:https://agupubs.onlinelibrary.wiley.com/doi/pdf/10.1029/2003JD004485.

Whitby, E., & McMurry, P. (1997). Modal aerosol dynamics modeling. *Aerosol Sci. Technol.*, *27*, 673–688.

Whitby, E., Stratmann, F., & Wilck, M. (2002). Merging and remapping modes in modal aerosol dynamics models: a "dynamic mode manager". *Journal of Aerosol Science*, *33*(4), 623–645. URL: https://www.sciencedirect.com/science/article/pii/S0021850201001975. doi:https://doi.org/10.1016/S0021-8502(01)00197-5.

Yamamoto, M., & Takahashi, M. (2006). An aerosol transport model based on a two-moment microphysical parameterization in the Venus middle atmosphere: Model description and preliminary experiments. *Journal of Geophysical Research (Planets)*, *111*, 8002. doi:10.1029/2006JE002688.

Yamamoto, M., & Tanaka, H. (1998). The venusian y-shaped cloud pattern based on an aerosol-transport model. *Journal of the Atmospheric Sciences*, *55*(8), 1400 – 1416. URL: https://journals.ametsoc.org/view/journals/atsc/55/8/1520-0469_1998_055_1400_tvyscp_2.0.co_2.xml. doi:10.1175/1520-0469(1998)055<1400:TVYSCP>2.0.CO;2.